

1 From random walks to fully anisotropic diffusion models for 2 cell and animal movement

3 Kevin J. Painter and Thomas Hillen

4 **Abstract** This chapter provides an introduction on how anisotropic diffusion models can be derived from
5 position-jump and velocity-jump random walks. We show how the availability of measurement data can
6 guide the choice of the appropriate model. We further present two new applications, respectively to cell
7 movement on micro-fabricated surfaces and magnetic compass orientation by sea turtle hatchlings.

8 1 Introduction

9 Getting from point A to point B is a daily challenge, although for the most part our movement patterns are
10 routine – staggering from bedroom to bathroom, from home to work, from office to coffee pot – and we
11 switch into autopilot, following the course hard-wired into our conscious. Sometimes we may find ourselves
12 in an unusual place attempting to reach an unfamiliar goal, yet even then navigation is straightforward when
13 armed with a smartphone and network connection.

14
15 Cells and animals do not have the technological aids at our disposal yet frequently need to migrate through
16 their environment, sometimes independently, sometimes collectively: the solo navigations of recently fledged
17 albatrosses across thousands of kilometres of southern oceans, or the collective movements of cells as they
18 move into developing tissues and organs offer particularly astonishing examples. Given the myriad of poten-
19 tial factors – chemicals, electric, magnetic and gravitational fields, topography and physical structure of the
20 environment, etc – a key question, whether posed by ecologists, cell biologists, microbiologists or oncolo-
21 gists, is exactly what cues signal to the cells or organisms along their paths.

22
23 Mathematical and computational modelling offer the means to address such questions, via encapsulating a
24 biological process into its essentials. Yet choosing an approach and setting up a model to begin with is far
25 from a trivial task. Inevitably this will come down to the knowledge and data we have and the nature of

K. J. Painter

Department of Mathematics and Maxwell Institute for Mathematical Sciences, Heriot-Watt University, UK & Dipartimento di Scienze Matematiche, Politecnico di Torino, Italy, e-mail: K.Painter@hw.ac.uk

T. Hillen

University of Alberta, Edmonton, Canada e-mail: thillen@ualberta.ca

26 the problem we are trying to address. One major determinant in the modelling choice will be the *biological*
27 *scale* of the problem. Consider a population-scale problem such as predicting the spatial spread of a cancer
28 to aid diagnosis and treatment. While we may have some understanding of the underlying biological pro-
29 cesses at a cellular level (e.g. enhanced proliferation and invasion of cells into healthy tissue), the primary
30 scale of interest is typically a macroscopic one at the time of treatment: the scale of the cancer (centimetres)
31 is significantly greater than the microscopic cells from which it is formed. In such instances, an efficient
32 and oft-used solution is to blur the population into a convenient density distribution and propose a suitable
33 evolution equation (such as a partial differential equation) for its change over space and time [48, 37, 36].

34
35 Macroscopic approaches such as these have formed a bedrock for mathematical modelling over many years,
36 providing insight into a wide variety of fundamental processes. When the only data we have is similarly
37 macroscopic, such as an MRI (magnetic resonance imaging) scan indicating the spatial extent of a cancer's
38 growth, a macroscopic model makes sense: fitting the model to approximated densities determined from the
39 scan offers a method of validation and parameter estimation [56]. But what if the available data is at the level
40 of the individual? Can we relate a model posed at a macroscopic level to an individual's movement? These
41 questions are clearly crucial when we consider technological advances in our capacity to track molecules,
42 cells or organisms: individual molecules can be tagged and followed via single particle tracking (SPT) as
43 they skate across the cell membrane [52]; labelled cells can be followed via sophisticated imaging while
44 migrating through a complicated tissue environment [59]; attaching a global positioning system (GPS) to
45 an animal can allow it to be followed even if it travels across oceans and continents [7]. Clearly, the data
46 provided by such methods can shed significant light on the fundamental mechanisms of movement. For
47 modellers, a significant challenge is raised: how can we best exploit all forms of available data to obtain
48 better models, both at the level of individuals and populations?

49
50 To motivate the rest of this chapter, we consider two very different applications respectively in cell move-
51 ment and turtle hatchling navigation. Both applications have a similar fundamental question (what are the
52 guidance cues that determine navigation?), but offer distinct examples for the type of data that may be at
53 hand for model parametrisation/formulation. In the case of cell movement we have a tabulated summary
54 of population-averaged behaviour. For turtles we have individual-level data, an orientation for each tested
55 hatchling in a sample. The analytical models we proceed to describe can be fitted to each of the datasets, in
56 each case shedding light on the problem.

57 ***1.1 Dataset A: Cell Movement on Microfabricated Substrates***

58 The development, maintenance and repair of our bodies requires that various cells migrate through com-
59 plex tissue environments; in tumour invasion, these same mechanisms can facilitate the rapid dispersal and
60 spread of malignant cells into neighbouring healthy tissue [19]. Various extracellular factors contribute to
61 cell guidance, ranging from extracellular molecules (e.g. chemoattractants and repellents), direct signals
62 from other cells (e.g. contact inhibition of locomotion) and the oriented movement of cells along aligned
63 structures [20, 42]. This latter form of oriented movement is generally termed contact guidance [14] and,
64 while principally described in the context of movement along the long bundles of collagen fibres charac-
65 teristic of connective tissue, can also occur during the movement of cells along axonal tracts of the central
66 nervous system or crawling along blood capillaries [17]. Contact guidance has been identified in various cell

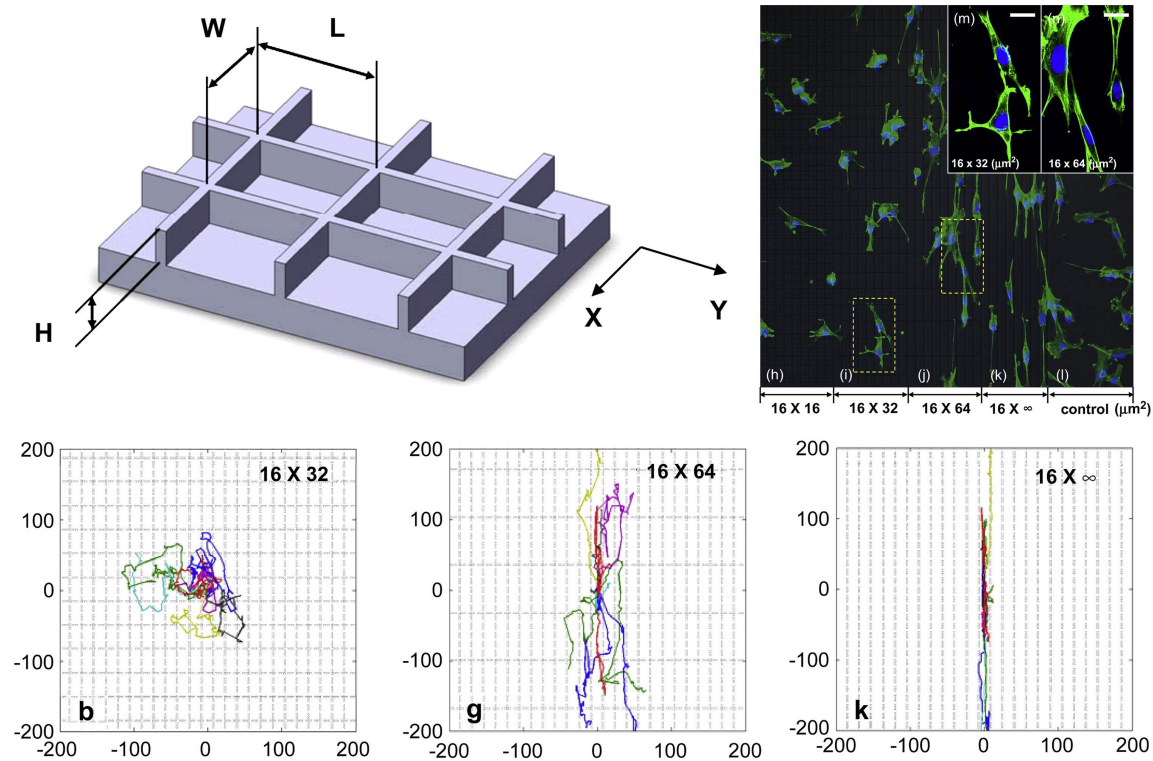


Fig. 1 Top Left: schematic of the micro-ridge substrate. Top Right: typical observation of cell movement on an anisotropic substrate, where the micro-ridges are in different aspect ratios. Bottom: cell tracks observed for different environmental anisotropies. Horizontal and vertical axes represent microns. Figures reprinted from *Biomaterials*, volume 31, Jeon, H., Hidai, H., Hwang, D.J., Healy, K.E. and Grigoropoulos, C.P., “The effect of micronscale anisotropic cross patterns on fibroblast migration”, pp. 4286–4295 (2010), with permission from Elsevier.

Case ($\mu\text{m} \times \mu\text{m}$)	Ridge height (μm)	x -velocity $v_x \pm \text{error}$ ($\mu\text{m}/\text{min}$)	y -velocity $v_y \pm \text{error}$ ($\mu\text{m}/\text{min}$)	Speed $\pm \text{error}$ ($\mu\text{m}/\text{min}$)
12 x 24	3	0.38 ± 0.015	0.58 ± 0.025	0.78 ± 0.027
12 x 48	3	0.28 ± 0.014	0.9 ± 0.045	1.01 ± 0.045
12 x ∞	3	0.08 ± 0.005	0.56 ± 0.029	0.59 ± 0.029
16 x 32	3	0.48 ± 0.021	0.65 ± 0.026	0.9 ± 0.03
16 x 64	3	0.31 ± 0.015	0.87 ± 0.038	1.0 ± 0.039
16 x ∞	3	0.12 ± 0.007	0.8 ± 0.036	0.84 ± 0.036
24 x 48	3	0.26 ± 0.015	0.42 ± 0.024	0.55 ± 0.027
24 x 96	3	0.2 ± 0.012	0.49 ± 0.02	0.58 ± 0.022
24 x ∞	3	0.12 ± 0.007	0.48 ± 0.027	0.52 ± 0.028
12 x 24	10	0.33 ± 0.016	0.46 ± 0.024	0.65 ± 0.026
12 x 48	10	0.18 ± 0.013	0.76 ± 0.044	0.83 ± 0.046
12 x ∞	10	0.04 ± 0.003	0.60 ± 0.032	0.61 ± 0.032
control	0	0.38 ± 0.019	0.41 ± 0.033	0.63 ± 0.025

Table 1 Reproduction of the movement data from Jeon et al. [25] for fibroblast cells migrating on a micro-ridged substratum.

67 populations, including fibroblasts [13], immune cells [59] and various cancerous populations [49, 16].

68

69 The capacity of environmental anisotropy to influence cell orientation/movement can be studied by tracing
70 cell paths when plated on micro-fabricated structures. To illustrate the data available from such experiments
71 we analyse those in Jeon et al. [25], where a two-dimensional substratum is formed with a rectangular array
72 of orthogonal micro-ridges, see Figure 1 (left). Inter-ridge lengths in the x - and y -directions are respec-
73 tively denoted W and L , with the former set at 12, 24 or 48 μm and the latter set to generate $W : L$ ratios of
74 $1 : 2$, $1 : 4$ or $1 : \infty$ (the last case corresponding to an absence of ridges in the x -direction). Ridge heights
75 were set at 3 μm , with further tests conducted at 10 μm and a control case without any ridges. NIH373
76 fibroblast cells were plated on these substrates: a population characterised by its mesenchymal movement
77 with cells extending long protrusions to probe the environment. Cells clearly align to the micro-ridges, gen-
78 erating anisotropic movement (see Figure 1, top right and bottom row) under anisotropic arrangements. Data
79 from individual tracking was summarised at a macroscopic level (averaged over the population) in terms of
80 mean speeds and directional bias, reproduced in Table 1. In Section 4.1 we will use this data to parametrise
81 an anisotropic diffusion model that describes cell spread for different anisotropies in the substratum.

82

83 ***1.2 Dataset B: Magnetic Navigation in Loggerhead Hatchlings***

84 Maritime navigation is undeniably hazardous. The frequent lack of visible landmass, turbulent currents and
85 dramatic meteorological conditions resulted in frequent positional misreckoning (and shipwrecking) during
86 the early ages of maritime traffic, stimulating governments of the time to propose prizes for a method of
87 accurately establishing longitudinal coordinates. John Harrison’s marine chronometer marked a pivotal mo-
88 ment in the transition towards (relatively) safe navigation [53]. Marine animals, of course, do not rely on
89 such aids but many species routinely undertake long marine journeys [29], with one of the most phenomenal
90 belonging to the loggerhead turtle (*Caretta caretta*). North Atlantic loggerhead hatchlings dash to the ocean
91 from eggs laid at various nesting beaches and undergo a period of “frantic” swimming that transports them
92 from the dangerous coastal waters to ocean circulatory currents such as the Gulf Stream. They subsequently
93 embark on a years to decades long period of open ocean migration, remaining within the warmer waters
94 of the Sargasso Sea and the North Atlantic Subtropical Gyre, the circular current system that surrounds it
95 (Figure 2). As adults, they continue to navigate between feeding grounds or back to nesting beaches.

96

97 Considering the small size of hatchlings and juveniles, sustained swimming is energetically demanding and
98 there is clear benefit to simply drifting within the convenient conveyor belt of the North Atlantic Gyre. Yet,
99 such simplistic behaviour could come with a risk if the stream branches, such as in the North Atlantic where
100 it splits into separate streams heading south (towards the warmer waters of the Azores) or north (into the
101 colder waters of Ireland and the North Atlantic), Figure 2; drifting into the latter could transport turtles into
102 perilously cold waters. Consequently, it is likely that some degree of positional awareness and navigation is
103 employed and an increasing volume of evidence has emerged on the potential for turtles to follow a mag-
104 netic compass [28], exploiting the information provided by the Earth’s magnetic field. Such a capacity would
105 clearly be advantageous: despite its diurnal and secular variation, magnetic field information is always avail-
106 able (unlike, say, celestial cues).

107

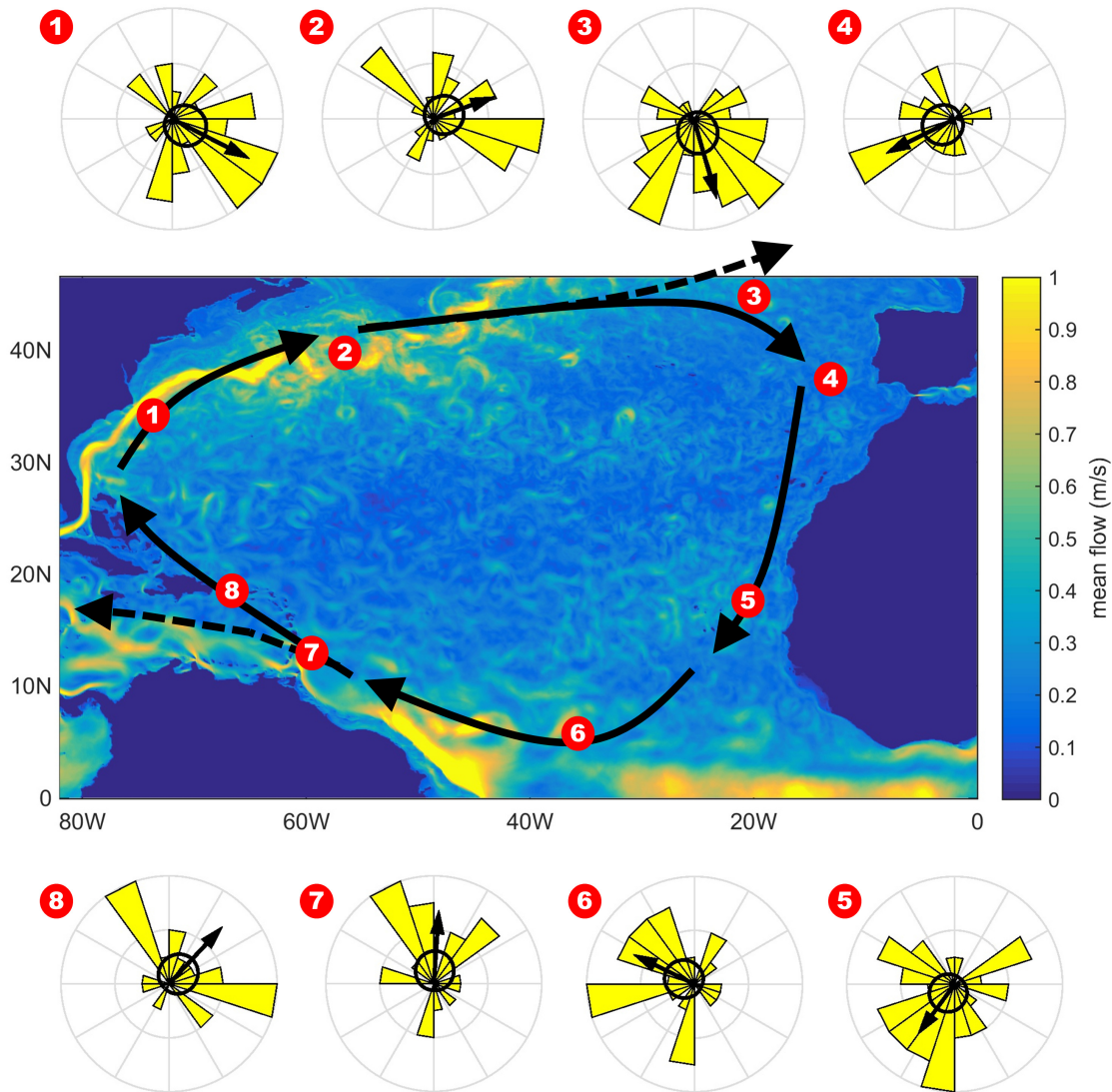


Fig. 2 The North Atlantic Gyre (Black arrows) is a circular system of currents, formed by the Gulf Stream, the North Atlantic Current, the Canary Current and the North Equatorial Current. For North Atlantic loggerhead turtles, such as those hatching along Florida beaches, remaining inside the region enclosed by the Gyre is optimal for access to suitable feeding grounds (e.g. the Sargasso Sea, the Azores) and to avoid straying into perilously cold waters (e.g. far North Atlantic) or unfamiliar geographic regions (far from traditional nesting/feeding sites). Two potentially hazardous points are indicated by the North Easterly point (3) and the South Westerly point (7): here, currents split into northerly/southerly streams for (3) and northerly/westerly streams for (7). Circular histograms reproduce the hatchling orientation data from [28], where (1-8) correspond to the locations where the magnetic field was reproduced in an experimental arena. When this data is fitted to the von Mises distribution, equation (11), a clear bias emerges, with the dominant direction and concentration strength reflected by the arrow direction and length (concentration parameters κ range from 0.67 for dataset 5 to 0.91 for dataset 1). Clearly, the unimodal von Mises distribution may not always be an “optimal” distribution: for example, datasets 2 and 8 may be more convincingly fitted by a multimodal form, such as linear combinations of von Mises distributions. Given the present study aims and the limited sample sizes, we restrict our fitting to the unimodal von Mises distribution.

108 To investigate this hypothesis, Lohmann and colleagues (see [28] for a review) devised a laboratory exper-
 109 iment that monitors how hatchling orientation changes when exposed to distinct magnetic fields. Briefly, a
 110 turtle is placed in a large water-tank while harnessed and tethered to an electronic monitor that computes its
 111 swimming direction. The tank is surrounded by a coil system capable of replicating specific geomagnetic
 112 fields, such as those found at distinct points along a turtles typical migratory route. Following an acclima-
 113 tisation period, the mean swimming direction over a 5 minute period is recorded for each turtle, generating
 114 orientation data at an individual level. In Figure 2 we reproduce the data summarised in [28] (itself sum-
 115 marising the collection of studies found in [27, 50, 15]). Specifically, magnetic fields were reproduced for
 116 different points along the North Atlantic Gyre and, for each location, the (mean) orientation of each tested
 117 turtle is binned into a circular histogram. The key inference from these studies is that hatchlings indeed show
 118 subtle changes to their preferred swimming direction, consistent with an orientation that optimises remain-
 119 ing within the Gyre. In Section 4.2 we will use this data to parametrise stochastic and continuous models,
 120 assessing the capacity for oriented swimming to maintain successful circulation of hatchlings.

121 **1.3 Outline**

122 In the next section (Section 2) we introduce advection-diffusion equations and the fully-anisotropic advection-
 123 diffusion framework. We introduce *position-jump* and *velocity-jump* random walks as two alternative
 124 stochastic models for oriented movement, and show how these models can be parametrised by translat-
 125 ing between individual-level and population-level measurements via circular statistics. In Section 3 we give
 126 detailed derivations of the fully-anisotropic advection-diffusion model, starting from either a position-jump
 127 or velocity-jump process. In Section 4 we return to the two applications/datasets described above. While
 128 each dataset offers a rather distinct set of summary statistics, we show how they can both be incorporated
 129 within our framework to parametrise models.

130 **2 Basic Tools**

131 Here we outline the basic set of tools that we employ to model and analyse population spread in an
 132 anisotropic/oriented environment: advection-diffusion equations, scaling limits for random walks, position-
 133 jump and velocity-jump random walks and directional statistics. We note that the derivations of the follow-
 134 ing sections require a copious notation, spanning scalar, vector and tensor/matrix quantities. To help the
 135 reader keep track, we use normal face fonts for scalar quantities (e.g. $t, p, u \dots$), bold faces for vectors (e.g.
 136 $\mathbf{a}, \mathbf{n}, \mathbf{v} \dots$) and double struck ($\mathbb{D}, \mathbb{V} \dots$) for tensors and matrices. Much of the material here is of an elementary
 137 textbook nature, and we limit references as follows: for more information on the use of advection-diffusion
 138 equations in biology, see for example [35, 37]; for more information and perspectives on random walks and
 139 their continuous approximations in biological systems, see for example [46, 38, 39, 47, 9, 41, 22]; for more
 140 information on the theory and use of directional statistics in biology, see [2, 31].

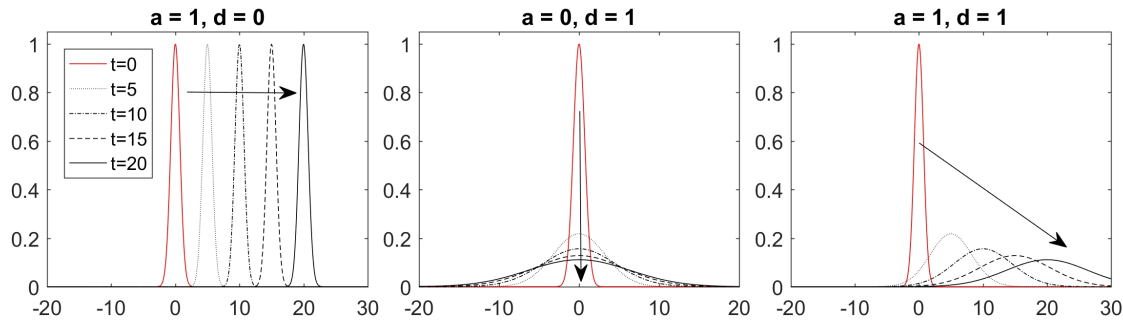


Fig. 3 Typical solutions of the basic diffusion-advection equation (1). Initial conditions are $u(x,0) = e^{-x^2}$ and solutions shown for (left to right): pure advection; pure diffusion; diffusion-advection.

141 2.1 Advection-Diffusion Equations

142 Advection-diffusion equations (AD equations) occupy a prominent position in biological movement mod-
 143 elling [35, 37]. Firstly, AD equations have a relatively straightforward and intuitive form and their long
 144 history has generated numerous methods for their analysis. Secondly, AD equations can arise as a limiting
 145 form from more realistic/detailed models: they can be derived from discrete and continuous random walks
 146 [38], from stochastic differential equations [18] and from individual based models [12]. Thirdly, they have
 147 shown to be powerful models capable of describing a wide range of applications in areas as diverse as mi-
 148 crobiology [11], ecology [34, 30], physiology [26], and medicine [45]. In short, AD equations describe the
 149 basic elements of a movement process.

150
 151 In the simplest case we restrict to a one-dimensional line and consider a constant drift velocity a and constant
 152 diffusion coefficient $d > 0$. The AD equation for some population density $u(x,t)$, where x denotes position
 153 along the line and t describes time, is given by

$$u_t + au_x = du_{xx} \quad (1)$$

154 where the index notation denotes partial derivatives.

155
 156 In the absence of diffusion ($d = 0$), we have $u_t + au_x = 0$ and solutions are of the form $u(x - at)$, describing
 157 movement with constant speed a . If $a > 0$ this movement is to the right and if $a < 0$ to the left (see Figure 3
 158 left). In the absence of advection ($a = 0$) we obtain a pure heat (or diffusion) equation $u_t = du_{xx}$: solutions
 159 disperse (Figure 3 middle) and (for $x \in \mathbb{R}$) the fundamental solution is

$$u(x,t) = \frac{1}{\sqrt{4\pi dt}} e^{-x^2/4dt}.$$

160 Taking both terms together ($a \neq 0, d > 0$) the population is transported with velocity a while simultaneously
 161 spreading due to diffusion (Figure 3 right).

162
 163 While the basic elements of directed movement (via a) and spatial spread (via d) are already contained in
 164 (1), questions arise concerning their specific choices related to biological observations/properties: How does

165 the direction and thickness of nano-grooves translate to advection/diffusion terms? How can we link datasets
 166 on turtle headings to these parameters? To answer questions like these we need to generalise the above AD
 167 equations (1) in a number of ways:

- 168 • advection and diffusion coefficients will more generally depend on space and time;
- 169 • we need to explore AD equations in higher space dimensions, in particular two dimensions for the exam-
 170 ples studied here;
- 171 • as we shall see, any underlying anisotropy or oriented information in the environment can affect both
 172 advection and diffusion, necessitating usage of an anisotropic formulation with $n \times n$ diffusion tensor
 173 $\mathbb{D}(\mathbf{x}, t)$.

174 Instead of (1) we will therefore consider the *fully anisotropic advection-diffusion equation* (FAAD equation):

$$u_t + \nabla \cdot (\mathbf{a}(\mathbf{x}, t)u) = \nabla \nabla : (\mathbb{D}(\mathbf{x}, t)u). \quad (2)$$

175 Note that because the advective velocity $(\mathbf{a}(\mathbf{x}, t))$ now depends on space, it appears inside the divergence
 176 such that $u_t + \nabla \cdot (\mathbf{a}(\mathbf{x}, t)u) = 0$ is a conservation law. The new anisotropic diffusion term in (2) demands
 177 special attention. The colon notation $(:)$ used here denotes the contraction of two tensors, and generates a
 178 summation across the full suite (i.e. including mixed) of second order derivatives:

$$\nabla \nabla : (\mathbb{D}(\mathbf{x}, t)u) = \sum_{i,j=1}^n \frac{\partial}{\partial x_i} \frac{\partial}{\partial x_j} (\mathbb{D}^{ij}(\mathbf{x}, t)u(\mathbf{x}, t)). \quad (3)$$

179 Note moreover that this term can be expanded into

$$\nabla \nabla : (\mathbb{D}u) = \nabla \cdot (\mathbb{D}\nabla u) + \nabla \cdot ((\nabla \cdot \mathbb{D})u),$$

180 which reveals a standard (Fickian-type) anisotropic diffusion term along with an advection term with velocity
 181 $\nabla \cdot \mathbb{D}$. As we will show below, the term (3) arises naturally from a detailed random walk description for
 182 moving biological agents. We also note that this term can confer some advantages over the standard Fickian
 183 anisotropic diffusion form $(\nabla \cdot (\mathbb{D}\nabla u))$: in particular, (3) can allow local maxima and minima to form in the
 184 population density steady state distribution, consistent with certain biological observations. Before we move
 185 on to this we first show how explicit expressions can be obtained for drift and diffusion terms, correlating to
 186 the inputs into an individual-level random walk, and introduce scaling methods in the process.

187 2.2 Scaling Limits for a Simple Random Walk

188 Consider an unfortunate hare confined to a life of consecutive and equispaced hops left or right along an
 189 infinite one-dimensional road. This animal's convenient movement path can be characterised by a probability
 190 density function $p(x, t)$, denoting the probability of the hare being at position x at time t . We set δ to be the
 191 hop length, q and $1 - q$ as the probabilities of a jump to the right or left and introduce τ as the (assumed
 192 constant) time between consecutive hops. To determine an equation for $p(x, t + \tau)$ we need to calculate the
 193 probability of finding the individual at x at time $= t + \tau$. Clearly this will only be possible if the individual
 194 has jumped right from position $x - \delta$, or left from $x + \delta$, at time t . As a result, we have the discrete *Master*
 195 *equation*

$$p(x, t + \tau) = qp(x - \delta, t) + (1 - q)p(x + \delta, t). \quad (4)$$

196 How can we determine a continuous limit for this discrete equation? The first step is to reinterpret p as a
 197 continuous probability distribution and then expand the left hand side about (x, t) as a function of t in powers
 198 of τ , and the right hand side terms as functions of x in powers of δ . After removing the arguments (x, t) for
 199 clarity, we find

$$p + \tau p_t + \frac{\tau^2}{2} p_{tt} + \dots = q \left(p - \delta p_x + \frac{\delta^2}{2} p_{xx} - \dots \right) + (1 - q) \left(p + \delta p_x + \frac{\delta^2}{2} p_{xx} + \dots \right),$$

200 where the subscripts denote partial derivatives. Simplifying, we obtain

$$p_t(x, t) = \frac{\delta}{\tau} (1 - 2q) p_x(x, t) + \frac{\delta^2}{2\tau} p_{xx}(x, t) + O\left(\tau, \frac{\delta^3}{2\tau}\right). \quad (5)$$

201 Glancing at Equation (5) hints at the continuous model, where we see that the *leading terms* form an
 202 advection-diffusion equation,

$$p_t(x, t) = -ap_x(x, t) + dp_{xx}(x, t) \quad (6)$$

203 with

$$a = \frac{\delta}{\tau} (2q - 1) \quad \text{and} \quad d = \frac{\delta^2}{2\tau}.$$

204 However, to do this more formally we must think carefully about different *scalings*, corresponding to distinct
 205 limiting scenarios as $\delta, \tau \rightarrow 0$ and $q \rightarrow 1/2$. We will present three choices: others certainly exist, yet the
 206 majority do not lead to a useful limit equation. In other words, if δ, τ and q do not scale as indicated below,
 207 then the above does not provide an appropriate method for deriving a useful continuous model. Note that for
 208 each of these scalings, all of the hidden lower order terms of equation (5) limit to zero and are henceforth
 209 excluded from consideration.

210 **(a)** Suppose $\delta, \tau \rightarrow 0$ such that $\frac{\delta}{\tau} \rightarrow \alpha = \text{constant}$. This describes a *hyperbolic scaling*. Hence, $\frac{\delta^2}{\tau} \rightarrow 0$,
 211 and the diffusive term vanishes. Thus, we are left with a simple *transport equation*

$$p_t + ap_x = 0,$$

212 where the advective velocity is $a = \alpha(2q - 1)$. We can see from this that the advective speed reaches a
 213 maximum of α when $q = 0$ or 1 , which corresponds to always choosing left or always choosing right: i.e.
 214 there will be no doubling back.

215 **(b)** Suppose $\delta, \tau \rightarrow 0$ such that $\frac{\delta^2}{\tau} \rightarrow 2d = \text{constant}$. This describes a *parabolic scaling*. Here we can
 216 consider two cases:

217 **(b.1)** If $q = \frac{1}{2}$. Here we have $a = 0$ and we hence obtain a pure *diffusion equation*

$$p_t = dp_{xx}.$$

218 **(b.2)** If $q \rightarrow \frac{1}{2}$ in such a way that $\frac{\delta}{\tau}(2q - 1) \rightarrow a$, and $\frac{\delta^2}{2\tau} \rightarrow d$, then the scaling results in the *advection-*
 219 *diffusion equation*

$$p_t + ap_x = dp_{xx}. \quad (7)$$

220 Summarising:

221 • When δ and τ scale in the same way, then we obtain a pure transport equation. This case is called *drift*
 222 *dominated*.

- 223 • When $\delta^2 \sim \tau$, we have the *diffusion dominated* case.
- 224 • Only if $q - \frac{1}{2} \sim \delta$ do we get both terms, an advection and a diffusion term (*mixed case*). In this case
- 225 we exactly derive our simple one-dimensional AD equation (1), but now we have a connection from the
- 226 macroscopic parameters a and d to the statistical inputs of the underlying random walk process (q, δ, τ) .

227 The question of which scaling to apply will typically come down to the appropriate relationship between the
 228 *macroscopic* and the *individual* spatial and temporal scales: i.e. between the scales of the individual move-
 229 ment process and the scale of the problem. For example, for the hops of a hare their frequency may take
 230 place on a timescale of seconds, over a distance of several centimetres. For modelling purposes, we may be
 231 interested in the dynamics of the system over observational scales ranging from minutes and metres to years
 232 and kilometres. The comparison between these scales provides the key to the appropriate scaling.

233
 234 It is important to note that we have, in fact, only derived a continuous limiting equation for the probability
 235 distribution of finding an individual at position x at time t . Can we directly relate p to a density function u that
 236 describes the distribution of a population? Formally, this would require that the jumpers are stochastically
 237 independent, i.e. that any interactions between population members can be (reasonably) ignored. This would,
 238 quite obviously, be a strong assumption if applied generally and its validity demands careful assessment
 239 [46, 54]. Accounting for population interactions will significantly complicate the proceedings (often to the
 240 point of intractability) and we shall therefore restrict to stochastically independent jumpers in the context of
 241 this chapter: effectively, we directly interchange the probability distribution p with the population density
 242 distribution u .

243 **2.3 Classes of Biological Random Walks**

244 In the above example we considered an *uncorrelated position-jump random walk on a discrete and regular*
 245 *one-dimensional lattice* for our underlying movement process: moves were uncorrelated, in that the decision
 246 of which direction to take did not depend on the previous decision(s), movement occurred through posi-
 247 tional jumps in space that ignored explicit description of passage between successive points, and were of
 248 fixed length, so that the path was localised to equally-spaced points along a one-dimensional line.

249
 250 More generally, two popular random walk descriptions for biological movement are the *position-jump* and
 251 *velocity-jump* random walk processes. These descriptions have been introduced to biological modelling by
 252 Othmer, Dunbar and Alt [38] and subsequently proven to be powerful and popular approaches. In the sim-
 253 pler position-jump process, the random walker jumps discretely from point to point according to certain
 254 jump probabilities (Figure 4 left); the one-dimensional random walk discussed above provides a particularly
 255 simple example. The more sophisticated velocity-jump process assumes piecewise continuous movement
 256 through space, with random walkers changing their velocity (or heading) during *turns*. Choosing an appro-
 257 priate random walk description involves a balancing of their respective advantages: for example, while the
 258 velocity-jump approach benefits from its more natural representation of biological movement, the subse-
 259 quent derivation of a continuous limiting equation is somewhat more complicated (Figure 4 right).

260

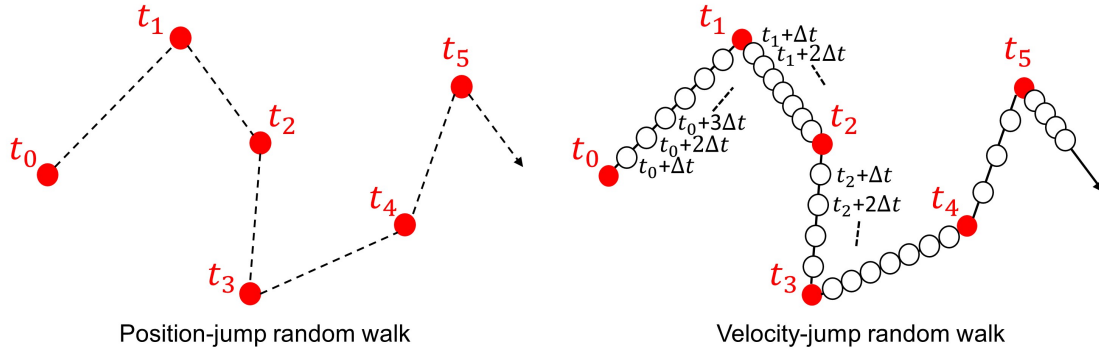


Fig. 4 Schematic illustrating position-jump and velocity-jump random walks. (Left) In the position-jump process, the particle makes instantaneous jumps through space at discrete times t_0, t_1, t_2, \dots (Right) In the velocity-jump process, the particle makes instantaneous velocity-changes at discrete times t_0, t_1, t_2, \dots (red circles), but subsequently moves continuously through space with a fixed velocity in the intervening times (white circles).

2.3.1 Position-Jump Processes

Moving beyond our simple random walk above, a more general position-jump random walk assumes movement proceeds through a sequence of positional jumps in space, interspersed according to some characteristic mean waiting time. Such instantaneous transitions are clearly somewhat unrealistic in the context of biological movement, yet given the discrete nature of many datasets (for example, satellite tracking of an animal in which its path is recorded through its spatial coordinate at discrete times) a position-jump model can often be justified as a reasonable approximation [5, 57].

Position-jump random walks can be alternatively stated via a discrete or continuous time master equation [38], and here we consider the former form. Specifically, we consider a population of stochastically independent jumpers performing a discrete time random walk, starting at $t = 0$ and making jumps at fixed times separated by time step τ . We introduce a redistribution kernel $K(\mathbf{y}, \mathbf{x}, t)$, a probability density function for a jump from position \mathbf{x} to \mathbf{y} at time t . Note that, as a probability, we have $K \geq 0$.

The difference in the population density at \mathbf{x} between times t and $t + \tau$ will be determined by summing all jumps into position \mathbf{x} and subtracting all those away from position \mathbf{x} , i.e. by the equation

$$u(\mathbf{x}, t + \tau) - u(\mathbf{x}, t) = \int_{D^{\mathbf{x}}} K(\mathbf{x}, \mathbf{y}, t) u(\mathbf{y}, t) - K(\mathbf{y}, \mathbf{x}, t) u(\mathbf{x}, t) d\mu(\mathbf{y}). \quad (8)$$

In the above, $(D^{\mathbf{x}}, \mu(\mathbf{y}))$ is a measure space. The above is general for random walks including jumps of various step lengths, or cases where movement occurs in continuous space or is restricted to discrete jumps between regularly or irregularly arranged nodes. The set $D^{\mathbf{x}}$ determines the set of destination/incoming sites for position \mathbf{x} , i.e. the set of points $\mathbf{y} \in D^{\mathbf{x}}$ from which jumps into or out of \mathbf{x} can be made, with $\mu(\mathbf{y})$ its associated measure. For example, if jumps can be made in any direction and any distance up to length h , then $D^{\mathbf{x}}$ becomes the ball centred on \mathbf{x} of radius h and the associated measure is the standard Lebesgue measure. If jumps can be made in any direction, but are restricted to a fixed length h , then $D^{\mathbf{x}}$ will be the sphere of radius h centred on \mathbf{x} and the associated measure is the surface Lebesgue measure. When movements become

285 restricted to a set of nodes, $D^{\mathbf{x}}$ becomes a finite or infinite set of discrete positions with a corresponding
 286 discrete measure.

287

288 The choice of redistribution kernel K is a key modelling decision, and allows various potential factors to
 289 be incorporated: for example, K could incorporate an impact due to environmental anisotropy or navigating
 290 cues that bias jumps into particular headings. The redistribution kernel is taken to be a probability measure,
 291 i.e.

$$\int_{D^{\mathbf{x}}} K(\mathbf{y}, \mathbf{x}, t) d\mu(y) = 1.$$

292 The above excludes spatio-temporal variation in the rate that jumps are made. However, it is noted that this is
 293 distinct from variation in staying at the same site, since $D^{\mathbf{x}}$ could include \mathbf{x} and remaining would correspond
 294 to $K(\mathbf{x}, \mathbf{x}, t) > 0$.

295 2.3.2 Velocity-Jump Processes

296 In velocity-jump random walks, movement consists of smooth runs with constant velocity interspersed by
 297 (instantaneous) reorientations [38]. For stochastically independent walkers, the individual-scale velocity-
 298 jump random walk can be formulated as an individual-scale continuous *transport equation*. Transport mod-
 299 els form a powerful and relatively new tool in the modelling and analysis of animal and cell movement
 300 [37, 21, 40, 47], although they have a long history in continuum mechanics (where they are usually referred
 301 to as kinetic equations) [8, 3]. As a result, various tools and techniques have been developed and in particu-
 302 lar the scaling techniques that allow their approximation to a reduced (and hopefully simpler) macroscopic
 303 model [47, 22]. Consequently, the transport equation can be thought of as a bridge that connects the individ-
 304 ual random walk to a fully continuous macroscopic model.

305

306 The reapplication of transport equations to biological processes has grown from seminal work of the 1980s
 307 (see [1, 38]) as an approach for modelling biological movement, whether by cells or organisms. Transport
 308 equations typically refer to mathematical models in which the particles of interest are structured by their
 309 position in space, time and velocity. In words, the transport equation for animal/cell movement takes the
 310 intuitively simple form:

$$\begin{array}{ccc} \text{Rate of change of population} & \text{Change due to} & \text{Change due to} \\ \text{moving with velocity } \mathbf{v} & \text{movement through} & \text{turning into or out} \\ \text{at position } \mathbf{x} \text{ time } t & \text{space} & \text{of velocity } \mathbf{v} \end{array} = \text{movement through} + \text{turning into or out}$$

311 Formally, if we define by $p(\mathbf{v}, \mathbf{x}, t)$ to be the density of the population moving with velocity $\mathbf{v} \in V$ at position
 312 \mathbf{x} and time t , then

$$p_t(\mathbf{v}, \mathbf{x}, t) + \mathbf{v} \cdot \nabla p(\mathbf{v}, \mathbf{x}, t) = \mathcal{L}p(\mathbf{v}, \mathbf{x}, t), \quad (9)$$

313 where \mathcal{L} denotes a *turning operator* that describes the process of velocity switching¹. For the velocity space
 314 $V \subset \mathbb{R}^n$ we take $V = [s_1, s_2] \times S^{n-1}$, where $0 \leq s_1 \leq s_2 < \infty$, s_1 and s_2 define the lower and upper bounds for
 315 organism movement speed² and S^{n-1} defines the unit sphere.

316

¹ We note that this particular form assumes there is no net force on the particles, and thus no inertia on them.

² It is worth noting that this is a key distinction from the kinetic theory of gas molecules, where $V = \mathbb{R}^n$ permits (at least theoretically) individual molecules to acquire infinite momentum [8].

317 The choice of \mathcal{L} forms a key modelling decision, and an oft-used form is the integral operator representation
 318 [38]:

$$\mathcal{L}p(\mathbf{v}, \mathbf{x}, t) = -\mu p(\mathbf{v}, \mathbf{x}, t) + \mu \int_V T(\mathbf{v}, \mathbf{v}', \mathbf{x}, t) p(\mathbf{v}', \mathbf{x}, t) d\mathbf{v}', \quad (10)$$

319 where the first term on the right hand side gives the rate at which particles switch away from velocity \mathbf{v}
 320 and the second term denotes the switching into velocity \mathbf{v} from all other velocities. The parameter μ is the
 321 *turning rate*, with $1/\mu$ the *mean run time* between individual turns. The turning kernel $T(\mathbf{v}, \mathbf{v}', \mathbf{x}, t) \geq 0$
 322 denotes the switching into velocity \mathbf{v} for a turn made at position \mathbf{x} and time t , given some previous velocity
 323 \mathbf{v}' . Mass conservation demands

$$\int_V T(\mathbf{v}, \mathbf{v}', \mathbf{x}, t) d\mathbf{v} = 1$$

324 and consequently T denotes a probability measure over V . As for the redistribution kernel in the position-
 325 jump process, its choice is a major consideration: for example orientation signals from the environment at \mathbf{x}
 326 and time t , or the inclusion of persistence in the previous direction \mathbf{v}' .

327 2.4 Directional Statistics

328 Each of the position-jump and velocity-jump processes above rely on various biological inputs: mean wait-
 329 ing times, speeds, turning rates and redistribution kernels. It is through these inputs that the random walk
 330 can be linked to biological datasets, and not least significant are the kernels K and T , which respectively de-
 331 scribe probability distribution functions for either the redistribution kernel for a positional jump from some
 332 position \mathbf{x} to a position \mathbf{y} , or a change of velocity from \mathbf{v}' to \mathbf{v} . Fundamentally, each distribution encapsu-
 333 lates an orientating “choice” of the animal or cell and we now turn to consider some suitable representations.

334
 335 Typical datasets for cell movement and animal navigation problems relate to orientations/headings in space
 336 and handling such data demands a review of some concepts from directional statistics [31]. In two dimen-
 337 sions, directional (or circular) statistics involves consideration of data on orientations that can be expressed
 338 with respect to some angle α relative to a given x -direction. The problem of directly transposing the defini-
 339 tions of regular (linear) statistics to circular statistics becomes immediately apparent with even its simplest
 340 concepts: for a set of angles uniformly distributed across the circle, what meaning would the (linear) mean
 341 angle of this dataset have?

342
 343 In general we consider the set of directions on the n -dimensional sphere, i.e. the set of unit vectors $\mathbf{n} \in S^{n-1}$.
 344 A directional distribution is then a probability distribution $q(\mathbf{n})$ defined over S^{n-1} , i.e. one satisfying

$$q(\mathbf{n}) \geq 0 \quad \text{and} \quad \int_{S^{n-1}} q(\mathbf{n}) d\mathbf{n} = 1.$$

345 Of particular importance for our work are the first and second moments of q , respectively the expectation \mathbf{E}_q
 346 and variance-covariance matrix \mathbb{V}_q (which we will often refer to simply as the variance):

$$\mathbf{E}_q = \int_{S^{n-1}} \mathbf{n} q(\mathbf{n}) d\mathbf{n},$$

$$\mathbb{V}_q = \int_{S^{n-1}} (\mathbf{n} - \mathbf{E}_q)(\mathbf{n} - \mathbf{E}_q)^T q(\mathbf{n}) d\mathbf{n}.$$

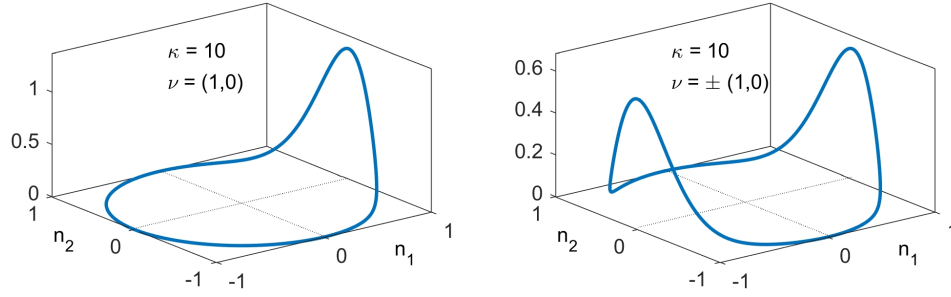


Fig. 5 Left: The unimodal von Mises distribution as a function of $\mathbf{n} = (n_1, n_2)^T \in S^1$ with a peak at $\mathbf{v} = (1, 0)^T$. Right: The bimodal von Mises distribution q_{vM} as a function of $\mathbf{n} \in S^1$ with peaks at $\mathbf{v} = \pm(1, 0)^T$. In these plots we set $\kappa = 10$.

347 In two dimensions, distributions will be defined on the unit circle, i.e. $\mathbf{n} \in S^1$. The simplest example is the
 348 uniform distribution, $q(\mathbf{n}) = \frac{1}{2\pi}$, although this has obviously limited usage in cases where data shows clear
 349 clustering/structure.

350

351 Given the enormous importance of the normal distribution in linear statistics, it is clearly desirable to
 352 define a similar concept for circular statistics. While the wrapped normal distribution offers the most direct
 353 analogue, the normal distribution's prominent position in circular statistics is filled instead by its sibling the
 354 *von Mises distribution* [31, 2], which benefits from its more analytically tractable form; the subtle differences
 355 between the wrapped normal and von Mises distribution are unlikely to be differentiated within the context
 356 of typical (noisy) biological datasets. Suppose we have some dominant/preferred direction $\mathbf{v} \in S^1$, then the
 357 von Mises distribution is given by

$$q_{vM}(\mathbf{n}, \mathbf{v}, \kappa) = \frac{1}{2\pi I_0(\kappa)} e^{\kappa \mathbf{n} \cdot \mathbf{v}} \quad (11)$$

358 for $\mathbf{n} \in S^1$. Here κ denotes the *concentration parameter* and $I_0(\kappa)$ ($I_j(\kappa)$) denotes the modified Bessel
 359 function of first kind of order 0 (order j). The von Mises distribution is illustrated in Figure 5 on the left.

360

361 It is, of course, equally possible to write down the von Mises distribution in terms of polar angles. Denoting
 362 α to be the angle of \mathbf{n} and ϕ to be the angle of \mathbf{v} (i.e. the *dominant angle*), then we can write

$$q_{vM}(\alpha, \phi, \kappa) = \frac{1}{2\pi I_0(\kappa)} e^{\kappa \cos(\alpha - \phi)}.$$

363 The above form is more common, particularly in the biological literature [32], but it is less useful for compu-
 364 tations and can be notationally more cumbersome. Hence we work with the coordinate free form (11) when
 365 possible.

366

367 As for the normal distribution on the line, the von Mises distribution on the circle is the workhorse of planar
 368 directional statistics [31, 2]. It can be derived from random walks, diffusion equations and energy principles,
 369 and has applications in earth sciences, physics, biology, medicine and elsewhere. It is used for data fitting
 370 and hypothesis testing of directional data, and we will use it here for our modelling of biological movement.
 371 The first and second moments of (11) have been computed in [23] (amongst elsewhere) and are given by

$$\mathbf{E}_{q_{vM}} = \frac{I_1(\kappa)}{I_0(\kappa)} \mathbf{v}; \quad (12)$$

$$\mathbb{V}_{q_{vM}} = \frac{1}{2} \left(1 - \frac{I_2(\kappa)}{I_0(\kappa)} \right) \mathbb{I}_2 + \left(\frac{I_2(\kappa)}{I_0(\kappa)} - \left(\frac{I_1(\kappa)}{I_0(\kappa)} \right)^2 \right) \mathbf{v}\mathbf{v}^T. \quad (13)$$

372 Note that \mathbb{I}_2 denotes the 2×2 identity matrix, and $\mathbf{v}\mathbf{v}^T$ denotes the dyadic product of two vectors (in tensor
373 notation $\mathbf{v} \otimes \mathbf{v}$).

374

375 Many biological datasets possess multimodal structure and we note that the von Mises distribution can be
376 extended to describe such instances, for example through simple linear combinations of (11); the moments
377 correspondingly follow from linear combinations of (12-13). A particularly useful case emerges for axially-
378 symmetric directional information, such as the spreading of cells along nanogrooves or animal movement
379 along linear environment structures such as seismic lines [33]. In such cases we can define a bimodal von
380 Mises distributions with equal sized local maxima at $\pm \mathbf{v}$. As shown in [23], we find that for given $\mathbf{v} \in S^1$
381 the bimodal von Mises distribution

$$q_{bvM}(\mathbf{n}, \mathbf{v}, \kappa) = \frac{1}{4\pi I_0(\kappa)} (e^{\kappa \mathbf{n} \cdot \mathbf{v}} + e^{-\kappa \mathbf{n} \cdot \mathbf{v}}), \quad (14)$$

382 has moments

$$\mathbf{E}_{q_{bvM}} = \mathbf{0}, \quad (15)$$

$$\mathbb{V}_{q_{bvM}} = \frac{1}{2} \left(1 - \frac{I_2(\kappa)}{I_0(\kappa)} \right) \mathbb{I}_2 + \frac{I_2(\kappa)}{I_0(\kappa)} \mathbf{v}\mathbf{v}^T. \quad (16)$$

383 An illustration of the bimodal von Mises distribution is shown in Figure 5 on the right.

384

385 For the present chapter we exclusively concentrate on two-dimensional applications, however it is worth
386 remarking that extensions can be made to three dimensions. The equivalent of the von Mises distribution in
387 three dimensions is called the *Fisher distribution* and is given by

$$q_F(\mathbf{n}, \mathbf{v}, \kappa) = \frac{\kappa}{4\pi \sinh(\kappa)} e^{\kappa \mathbf{n} \cdot \mathbf{v}}, \quad \mathbf{n} \in S^2. \quad (17)$$

388 Again, first and second moments have been previously calculated for this distribution (see [23]), given by

$$\mathbf{E}_{q_F} = \left(\coth \kappa - \frac{1}{\kappa} \right) \mathbf{v}, \quad (18)$$

$$\mathbb{V}_{q_F} = \left(\frac{\coth \kappa}{\kappa} - \frac{1}{\kappa^2} \right) \mathbb{I} + \left(1 - \frac{\coth \kappa}{\kappa} + \frac{2}{\kappa^2} - \coth^2 \kappa \right) \mathbf{v}\mathbf{v}^T. \quad (19)$$

389 3 Derivation of Fully Anisotropic Advection-Diffusion Equations

390 Here we present two derivations of the FAAD model (2), respectively from a position-jump and velocity-
391 jump process. We will find that both the macroscopic drift velocity \mathbf{a} and the diffusion tensor \mathbb{D} depend

392 on statistical properties of the parameters in the corresponding random walk model. Hence, the choice of
 393 an appropriate model can be linked to the available data: if we can compute mean and variance of species
 394 locations, then the position-jump framework applies (see our cell movement example); if the data allow
 395 estimates for mean speeds, mean directions and their variances, then the velocity-jump process is perhaps a
 396 better choice (see the sea-turtle example).

397 **3.1 Position-Jump Derivation**

398 For the position-jump derivation we will make a number of convenient restrictions:

- 399 1. we assume random walks in which the jumps can occur in any direction (i.e. lattice-free), but are restricted
 400 to fixed length δ .
- 401 2. we assume the jump is *myopic* (or short-sighted).

402 The first restriction determines that the set D in equation (8) simply becomes the sphere of radius δ . The
 403 myopic nature of the jump implies that the heading is based only on environmental information obtained at
 404 the present site, i.e. at (\mathbf{x}, t) for a walker at position \mathbf{x} at time t ; alternatives could involve, as an example, a
 405 dependence on information at the destination site, or a comparison between the current and destination site
 406 [55].

407
 408 The consequence of these assumptions is that our redistribution kernels can be written in terms of a direc-
 409 tional distribution for choosing direction $\mathbf{n} \in S^{n-1}$, i.e. $K(\mathbf{y}, \mathbf{x}, t) = k(\mathbf{n}, \mathbf{x}, t)$ where \mathbf{n} is in the direction $\frac{\mathbf{y}-\mathbf{x}}{|\mathbf{y}-\mathbf{x}|}$
 410 and the Master equation becomes

$$u(\mathbf{x}, t + \tau) - u(\mathbf{x}, t) = \int_{S^{n-1}} k(\mathbf{n}, \mathbf{x} - \delta \mathbf{n}, t) u(\mathbf{x} - \delta \mathbf{n}, t) - k(\mathbf{n}, \mathbf{x}, t) u(\mathbf{x}, t) d\mathbf{n}. \quad (20)$$

411 At this point it is interesting to quickly consider the connection to the one-dimensional case (4) that was
 412 studied earlier. In the one-dimensional case we have only two headings, $\mathbf{n} \in \{-1, 1\}$. Hence we define

$$k(\mathbf{n}, x, t) = q\delta_0(-1 - \mathbf{n}) + (1 - q)\delta_0(1 - \mathbf{n}),$$

413 where δ_0 denotes the Dirac-delta distribution. Then (20) becomes

$$u(x, t + \tau) = qu(x - \delta, t) + (1 - q)u(x + \delta, t),$$

414 which is exactly (4).

415

416 For small values of δ and τ we expand the right hand side of equation (20) about \mathbf{x} and the left hand side
 417 about t to obtain

$$\begin{aligned} \frac{\partial u}{\partial t} + O(\tau) &= \frac{\delta}{\tau} \int_{S^{n-1}} -\mathbf{n} \cdot \nabla (ku) + \frac{\delta}{2} (\mathbf{n} \cdot \nabla)^2 (ku) + O(\delta^2) d\mathbf{n}, \\ &= -\frac{\delta}{\tau} \left(\nabla \cdot \int_{S^{n-1}} k \mathbf{n} d\mathbf{n} \right) u + \frac{\delta^2}{2\tau} \left(\nabla \nabla : \int_{S^{n-1}} \mathbf{n} \mathbf{n}^T k d\mathbf{n} \right) u + O(\delta^3/\tau), \end{aligned}$$

418 where we use the colon notation ($:$) which denotes the contraction of two tensors as

$$A : B = \sum_{i,j=1}^n a_{ij} b_{ij}, \quad A, B \in \mathbb{R}^{n \times n}.$$

419 As discussed in Section 2.2, distinct scalings generate different continuous limits and we again consider both
420 the drift and diffusion dominated scenarios.

421 • (drift dominated) if $\delta, \tau \rightarrow 0$ such that $\lim_{\delta, \tau \rightarrow 0} \frac{\delta}{\tau} = c$ (constant) we have the hyperbolic model

$$\frac{\partial u}{\partial t} + \nabla \cdot (\mathbf{a}(\mathbf{x}, t)u) = 0,$$

422 where $\mathbf{a}(\mathbf{x}, t) = c \int_{S^{n-1}} \mathbf{n} k(\mathbf{n}, \mathbf{x}, t) d\mathbf{n}$ (i.e. the advection is proportional to the first moment of k).

423 • if $\delta, \tau \rightarrow 0$ such that $\lim_{\delta, \tau \rightarrow 0} \frac{\delta^2}{2\tau} = d$ then we have two cases

424 – (diffusion dominated) if $\int_{S^{n-1}} \mathbf{n} k d\mathbf{n} = 0$ then we have

$$\frac{\partial u}{\partial t} = \nabla \nabla : (\mathbb{D}(\mathbf{x}, t)u),$$

425 where $\mathbb{D}(\mathbf{x}, t)$ is the $n \times n$ matrix defined by $\mathbb{D}(\mathbf{x}, t) = d \int_{S^{n-1}} \mathbf{n} \mathbf{n}^T k(\mathbf{n}, \mathbf{x}, t) d\mathbf{n}$.

426 – (drift-diffusion) If $\lim_{\delta, \tau \rightarrow 0} \frac{\delta^2}{2\tau} = d$ and $\lim_{\delta, \tau \rightarrow 0} \frac{\delta}{\tau} \int_{S^{n-1}} \mathbf{n} k d\mathbf{n} \sim c\delta$ we have

$$\frac{\partial u}{\partial t} + \nabla \cdot (\mathbf{a}(\mathbf{x}, t)u) = \nabla \nabla : (\mathbb{D}(\mathbf{x}, t)u),$$

427 with

$$\begin{aligned} \mathbf{a}(\mathbf{x}, t) &= c \int_{S^{n-1}} \mathbf{n} k(\mathbf{n}, \mathbf{x}, t) d\mathbf{n}, \\ \mathbb{D}(\mathbf{x}, t) &= d \int_{S^{n-1}} (\mathbf{n} - \mathbf{a}(\mathbf{x}, t)) (\mathbf{n} - \mathbf{a}(\mathbf{x}, t))^T k(\mathbf{n}, \mathbf{x}, t) d\mathbf{n}. \end{aligned}$$

428 The final form is particularly relevant, as it is exactly the FAAD model we introduced earlier. In this case, we
429 now have a connection to the advection velocity and diffusion tensor terms from the underlying statistical
430 inputs $k(\mathbf{n}, \mathbf{x}, t)$ of a random walk process.

431 3.2 Velocity-Jump Derivation

432 To facilitate the derivation we consider a simplified form of transport equation. Specifically, we assume that
433 the turning kernel does not depend on the previous velocity \mathbf{v}' , i.e.

$$T(\mathbf{v}, \mathbf{v}', \mathbf{x}, t) = T(\mathbf{v}, \mathbf{x}, t).$$

434 Using this choice in (10) for (9) we have the considerably simpler form

$$p_t(\mathbf{v}, \mathbf{x}, t) + \mathbf{v} \cdot \nabla p(\mathbf{v}, \mathbf{x}, t) = -\mu p(\mathbf{v}, \mathbf{x}, t) + T(\mathbf{v}, \mathbf{x}, t)u(\mathbf{x}, t), \quad (21)$$

435 where we have defined the macroscopic density

$$u(\mathbf{x}, t) = \int_V p(\mathbf{v}, \mathbf{x}, t) d\mathbf{v}. \quad (22)$$

436 The process from here is to derive an evolution equation for the macroscopic density $u(\mathbf{x}, t)$, which can be
 437 achieved through a variety of scaling techniques, including parabolic scaling, hyperbolic scaling and moment
 438 closure. For a detailed treatment for model (21) we refer to our earlier paper [22] and we summarise one
 439 such choice here: moment closure.

440 3.2.1 Moment Closure Method

441 In a moment closure approach, the idea is to identify statistically meaningful quantities related to p and
 442 T , such as expectations and variances. We remind ourselves that the formulation demands that the turning
 443 distribution $T(\mathbf{v}, \mathbf{x}, t)$ is a probability measure, i.e.

$$T(\mathbf{v}, \mathbf{x}, t) \geq 0, \quad \int_V T(\mathbf{v}, \mathbf{x}, t) d\mathbf{v} = 1,$$

444 and we consider its expectation \mathbf{E}_T and variance \mathbb{V}_T ,

$$\mathbf{E}_T(\mathbf{x}, t) = \int_V \mathbf{v} T(\mathbf{v}, \mathbf{x}, t) d\mathbf{v}, \quad \mathbb{V}_T(\mathbf{x}, t) := \int_V (\mathbf{v} - \mathbf{E}_T(\mathbf{x}, t))(\mathbf{v} - \mathbf{E}_T(\mathbf{x}, t))^T T(\mathbf{v}, \mathbf{x}, t) d\mathbf{v}. \quad (23)$$

445 $\mathbf{E}_T(\mathbf{x}, t)$ describes the mean new velocity vector for the turning kernel, while $\mathbb{V}_T(\mathbf{x}, t)$ is its variance-
 446 covariance matrix.

447

448 We now introduce the same quantities for $p(\mathbf{v}, \mathbf{x}, t)$, although we note that p in itself is not a probability
 449 measure, since $\int_V p(\mathbf{v}, \mathbf{x}, t) d\mathbf{v} = u(\mathbf{x}, t)$ is not necessarily equal to one. But we can normalise, introducing \hat{p}
 450 via the equation

$$u(\mathbf{x}, t) \hat{p}(\mathbf{v}, \mathbf{x}, t) = p(\mathbf{v}, \mathbf{x}, t)$$

451 and noting that $\int_V \hat{p}(\mathbf{v}, \mathbf{x}, t) d\mathbf{v} = 1$. We subsequently introduce the expectation and variances

$$\begin{aligned} \mathbf{E}_{\hat{p}}(\mathbf{x}, t) &= \int_V \mathbf{v} \hat{p}(\mathbf{v}, \mathbf{x}, t) d\mathbf{v}, \\ \mathbb{V}_{\hat{p}}(\mathbf{x}, t) &= \int_V (\mathbf{v} - \mathbf{E}_{\hat{p}}(\mathbf{x}, t))(\mathbf{v} - \mathbf{E}_{\hat{p}}(\mathbf{x}, t))^T \hat{p}(\mathbf{v}, \mathbf{x}, t) d\mathbf{v}. \end{aligned}$$

452 Then, $\mathbf{E}_{\hat{p}}$ defines the mean velocity of the normalized population while $\mathbb{V}_{\hat{p}}$ is its variance-covariance matrix.

453 In terms of the original population density p , we can write

$$\int_V \mathbf{v} p(\mathbf{v}, \mathbf{x}, t) d\mathbf{v} = \mathbf{E}_{\hat{p}}(\mathbf{x}, t) u(\mathbf{x}, t), \quad (24)$$

$$\int_V (\mathbf{v} - \mathbf{E}_{\hat{p}}(\mathbf{x}, t))(\mathbf{v} - \mathbf{E}_{\hat{p}}(\mathbf{x}, t))^T p(\mathbf{v}, \mathbf{x}, t) d\mathbf{v} = \mathbb{V}_{\hat{p}}(\mathbf{x}, t) u(\mathbf{x}, t). \quad (25)$$

454 Next we explain the moment closure method itself. We can derive equations for the expectation and variance
 455 introduced above, and it turns out that the equation for the expectation (first moment) depends on the variance
 456 (second moment) while the equation for the variance depends on a third moment etc. Effectively we obtain
 457 an infinite hierarchy of moment equations, where each new equation depends on a next higher moment. To

458 obtain a usable model, the sequence of equations must be cut somewhere, a process termed *moment closure*.
 459 Generally, choosing the right closure condition is a work of art and many plausible approaches are available
 460 in the literature [8, 20]. Here we will choose a standard method that uses the equilibrium distribution and cut
 461 at the second moment to obtain a single equation of type (2) for the mass density $u(\mathbf{x}, t)$.

462
 463 Let us start by integrating equation (21) over V and express each term with respect to the corresponding
 464 moments. Note that hereon we omit the arguments for readability.

$$\int_V p_t d\mathbf{v} + \int_V \nabla \cdot \mathbf{v} p d\mathbf{v} = -\mu \int_V p d\mathbf{v} + \mu \int_V T d\mathbf{v} u,$$

465 which can equivalently be written as

$$u_t + \nabla \cdot (\mathbf{E}_{\hat{p}} u) = -\mu u + \mu u = 0.$$

466 Hence our first equation is a conservation law

$$u_t + \nabla \cdot (\mathbf{E}_{\hat{p}} u) = 0. \quad (26)$$

467 As a next step we multiply (21) by \mathbf{v} and again integrate over V . We obtain

$$\int_V \mathbf{v} u_t d\mathbf{v} + \int_V \mathbf{v} (\nabla \cdot \mathbf{v} p) d\mathbf{v} = -\mu \int_V \mathbf{v} p d\mathbf{v} + \mu \int_V \mathbf{v} T d\mathbf{v} u,$$

468 which can be equivalently written as

$$(\mathbf{E}_{\hat{p}} u)_t + \nabla \cdot \int_V \mathbf{v} \mathbf{v}^T p d\mathbf{v} = \mu (\mathbf{E}_T - \mathbf{E}_{\hat{p}}) u. \quad (27)$$

469 We write the second moment $\int \mathbf{v} \mathbf{v}^T p d\mathbf{v}$ in terms of the variance of \hat{p} , i.e.

$$\begin{aligned} \mathbb{V}_{\hat{p}} u &= \int_V (\mathbf{v} - \mathbf{E}_{\hat{p}})(\mathbf{v} - \mathbf{E}_{\hat{p}})^T p d\mathbf{v}, \\ &= \int_V \mathbf{v} \mathbf{v}^T p d\mathbf{v} - 2 \int_V \mathbf{v} \mathbf{E}_{\hat{p}}^T p d\mathbf{v} + \mathbf{E}_{\hat{p}} \mathbf{E}_{\hat{p}}^T u. \end{aligned}$$

470 Hence

$$\int_V \mathbf{v} \mathbf{v}^T p d\mathbf{v} = \mathbb{V}_{\hat{p}} u + \mathbf{E}_{\hat{p}} \mathbf{E}_{\hat{p}}^T u.$$

471 We use this expression in (27) and obtain the equation for the expectation:

$$(\mathbf{E}_{\hat{p}} u)_t + \nabla \cdot (\mathbf{E}_{\hat{p}} \mathbf{E}_{\hat{p}}^T u) = -\nabla \cdot (\mathbb{V}_{\hat{p}} u) + \mu (\mathbf{E}_T - \mathbf{E}_{\hat{p}}) u. \quad (28)$$

472 So far we have simply integrated and introduced a few fancy variables for $\mathbf{E}_{\hat{p}}$, $\mathbb{V}_{\hat{p}}$ etc. The next step is to
 473 present two critical assumptions that allow us to close the system:

474 **(a1) Moment closure** – the variance $\mathbb{V}_{\hat{p}}$ is computed from the equilibrium distribution p_e : $\mathbb{V}_{\hat{p}} \approx \mathbb{V}_{\hat{p}_e}$.

475

476 **(a2) Fast flux relaxation** – the equation (28) for the expectation $\mathbf{E}_{\hat{p}}$ is in quasi-equilibrium.

477 It is noted that the above assumptions were originally conceived in a physical context, namely the kinetic
 478 theory of dilute gases [8]. The extent to which these can be directly translated to biological particles, such
 479 as cells and organisms, is uncertain and a goal for further investigations: within the present article we sim-
 480 ply take them as stated. The first assumption has proven to be useful in a number of studies. The second
 481 assumption effectively stipulates that, *at the space/time scales* of the macroscopic model, the particle instan-
 482 taneously respond to local information: reasonable, say, for an organism switching direction multiple times
 483 a day but studied over a macroscopic scale of months to years.

484 The equilibrium distribution p_e can be computed from the condition $\mathcal{L}p_e = 0$ where \mathcal{L} is the integral
 485 operator from (10). In our case

$$\mathcal{L}p = \mu(Tu - p) = 0$$

486 is solved by the equilibrium distribution ,

$$p_e(\mathbf{v}, \mathbf{x}, t) = u(\mathbf{x}, t)T(\mathbf{v}, \mathbf{x}, t).$$

487 This equilibrium distribution has the expectation

$$\mathbf{E}_{\hat{p}_e}u = \int_V \mathbf{v}p_e d\mathbf{v} = \int_V \mathbf{v}uT d\mathbf{v} = \mathbf{E}_T u. \quad (29)$$

488 Now we approximate the highest order term, the variance as

$$\mathbb{V}_{\hat{p}} \approx \mathbb{V}_{\hat{p}_e} = \int_V (\mathbf{v} - \mathbf{E}_{\hat{p}_e})(\mathbf{v} - \mathbf{E}_{\hat{p}_e})^T uT d\mathbf{v} = \mathbb{V}_T u. \quad (30)$$

489 In assumption (a2) we postulate that the equation (28) is in quasi steady state, i.e.

$$\mathbf{0} \approx -\nabla \cdot (\mathbb{V}_{\hat{p}}u) + \mu(\mathbf{E}_T - \mathbf{E}_{\hat{p}})u,$$

490 and, substituting the moment closure (30), we find the approximation

$$\mathbf{E}_{\hat{p}}u \approx -\frac{1}{\mu} \nabla \cdot (\mathbb{V}_T u) + \mathbf{E}_T u. \quad (31)$$

491 Finally, we substitute (31) into the conservation law (26) and we assume that the approximation is good (i.e.
 492 we replace \approx with $=$) to obtain a closed system

$$u_t + \nabla \cdot (\mathbf{E}_T u) = \frac{1}{\mu} \nabla \nabla : (\mathbb{V}_T u). \quad (32)$$

493 This closed equation is exactly the fully anisotropic advection-diffusion equation (FAAD) in (2) with

$$\mathbf{a}(\mathbf{x}, t) = \mathbf{E}_T(\mathbf{x}, t) \quad \text{and} \quad \mathbb{D}(\mathbf{x}, t) = \frac{1}{\mu} \mathbb{V}_T(\mathbf{x}, t). \quad (33)$$

494 Let us consider two special cases of this derivation.

495

496 **Example 1: (directional distributions)** Some further simplifications can be used to relate turning directly
 497 to a directional distribution. Let us restrict movement to a single speed, i.e. $V = sS^{n-1}$, where s is the mean
 498 speed and S^{n-1} is the n -dimensional sphere. Hence, $\mathbf{v} = s\mathbf{n}$ where $\mathbf{n} \in S^{n-1}$ defines the directional heading.

499 We can therefore simply define T in terms of a directional distribution, say q , for choosing some heading
500 $\mathbf{n} \in S^{n-1}$. Specifically,

$$T(\mathbf{v}, \mathbf{x}, t) := \frac{q(\mathbf{n}, \mathbf{x}, t)}{s^{n-1}}, \quad (34)$$

501 where the s^{n-1} factor results from moving between a distribution over V to one over S^{n-1} . Subsequently,
502 advection and diffusion tensors for (2) will be given by

$$\mathbf{a}(\mathbf{x}, t) = s\mathbf{E}_q(\mathbf{x}, t) = s \int_{S^{n-1}} \mathbf{n}q(\mathbf{n}, \mathbf{x}, t)d\mathbf{n}, \quad (35)$$

$$\mathbb{D}(\mathbf{x}, t) = \frac{s^2}{\mu} \mathbb{V}_q(\mathbf{x}, t) = \frac{s^2}{\mu} \int_{S^{n-1}} (\mathbf{n} - \mathbf{E}_q)(\mathbf{n} - \mathbf{E}_q)^T q d\mathbf{n}. \quad (36)$$

503 Notice that for the von-Mises and Fisher distributions discussed earlier, we have already computed expecta-
504 tion and variances: i.e. they are ready to be used.

505

506 **Example 2: (including external drift)** The above derivation can also be applied to the case of particles that
507 are drifting in an external velocity field $\mathbf{b}(\mathbf{x}, t) \in \mathbb{R}^n$, for example turtles transported in ocean currents or
508 insects blown by the wind. If particles are inactive their heading is exactly the direction of the external flow
509 field $\mathbf{b}(\mathbf{x}, t)$, in which case the directional distribution used for the turning kernel would be a point measure

$$T(\mathbf{v}, \mathbf{x}, t) = \delta_{\mathbf{b}(\mathbf{x}, t)}(\mathbf{v}).$$

510 Then, expectation and variances can be calculated as

$$\mathbf{E}_T(\mathbf{x}, t) = \mathbf{b}(\mathbf{x}, t) \quad \text{and} \quad \mathbb{V}_T(\mathbf{x}, t) = 0.$$

511 The above macroscopic limit is a pure drift equation

$$u_t + \nabla \cdot (\mathbf{b}(\mathbf{x}, t)u) = 0. \quad (37)$$

512 Note that the same equation arises if we simply assume that a force proportional to \mathbf{b} acts on cells, where
513 the cells have no inertia. In that case we also get a drift of the form $\mathbf{b}(x, t)$. For situations in which we have
514 a population of actively navigating/moving particles immersed in an external velocity field we can simply
515 combine the two cases of (35), (36) and (37) to obtain

$$u_t + \nabla \cdot ((\mathbf{a}(\mathbf{x}, t) + \mathbf{b}(\mathbf{x}, t))u) = \nabla \nabla : (\mathbb{D}(\mathbf{x}, t)u). \quad (38)$$

516 Indeed, this case was used to analyse sea turtle data in [43].

517 4 Applications to Cell/Animal Orientation Datasets

518 We illustrate the methodology through our two motivating applications. In each case we take as a start-
519 ing point an individual-based description for oriented movement: an underlying velocity-jump process for
520 the random walk. This initial description arises naturally, given our fundamental knowledge of particle be-
521 haviours: cells on fabricated substrates reveal alignment and orientation according to the substrate anisotropy

522 (Figure 1); datasets for turtles are based according to their mean swimming orientation when subjected to
 523 specific magnetic fields (Figure 2). We remark that in each application a two-dimensional approximation
 524 ($n = 2$) is reasonable: cells migrate across the two-dimensional substrate and the diving capabilities of young
 525 turtles restrict their movements to the ocean surface [10]. Simulation methods are provided in the Appendix.

526 The two applications differ not only in their field of study but also with respect to the “usable data”.
 527 For cell movement we consider a tabulated summary of responses for distinct micro-ridge substrates, Table
 528 1. This is data at a population-averaged level, and we do not have explicit data on each individual cell’s
 529 orientating response. Nevertheless, we can still use this data to directly parametrise our model, which is done
 530 directly at the FAAD level that arises as a continuous approximation of the individual model. In the case of
 531 hatchling movements, a circular dataset is available for the mean heading of each tested turtle in samples
 532 exposed to distinct navigation fields. In this case, we can directly parametrise the von Mises distribution that
 533 describes an individual’s orientation response, and subsequently scale to a macroscopic FAAD equation in
 534 order to collect population-level measurements.

535 **4.1 Application A: Cell Movement on Microfabricated Structures**

536 The data of Jeon et al. [25] in Table 1 are at a population level: the mean x -velocity ($v_x \pm v_{x,error}$), mean
 537 y -velocity ($v_y \pm v_{y,error}$) and mean speed ($s \pm s_{error}$), where velocity components are measured according to
 538 absolute values. To relate these to the parametrisation of (2), we first remark on some particulars induced by
 539 the anisotropic arrangement. Firstly, the dominant drift velocity $\mathbf{a} = 0$, since the environment is essentially
 540 bidirectional and, on average, equal numbers of cells will be found travelling up or down (left or right).
 541 Secondly, the substratum is anisotropic but spatially homogeneous, and hence the diffusion tensor \mathbb{D} is
 542 constant in space. Finally, anisotropies coincide with the coordinate axes, so \mathbb{D} becomes a diagonal matrix

$$\mathbb{D} = \begin{pmatrix} \lambda_x & 0 \\ 0 & \lambda_y \end{pmatrix}, \quad (39)$$

543 with two eigenvalues λ_x and λ_y .

544
 545 Given that \mathbb{D} is constant in space, the fully-anisotropic diffusion model becomes identical to the standard
 546 anisotropic diffusion equation:

$$u_t = \nabla \cdot \mathbb{D} \nabla u. \quad (40)$$

547 Hence we can exploit results relating to the above. Firstly, the fundamental solution of (40) is the Gaussian
 548 distribution with covariance matrix \mathbb{D} :

$$u(\mathbf{x}, t) = \frac{1}{2\pi t \sqrt{\text{Det}\mathbb{D}}} \exp\left(-\frac{1}{4t} \mathbf{x}^T \mathbb{D}^{-1} \mathbf{x}\right) \quad (41)$$

549 (in two spatial dimensions), where the set

$$E_c := \{\mathbf{x} : \mathbf{x}^T \mathbb{D}^{-1} \mathbf{x} = c\}$$

550 gives the set of locations for which there is an equal probability of finding a random mover that started at the
 551 origin. This set defines a *diffusion ellipse*, with semi-axes of lengths $\sqrt{\lambda_x}$ and $\sqrt{\lambda_y}$ respectively, and provides
 552 one way to graphically visualise the anisotropy of \mathbb{D} . A second method is the *diffusion peanut*, which is the

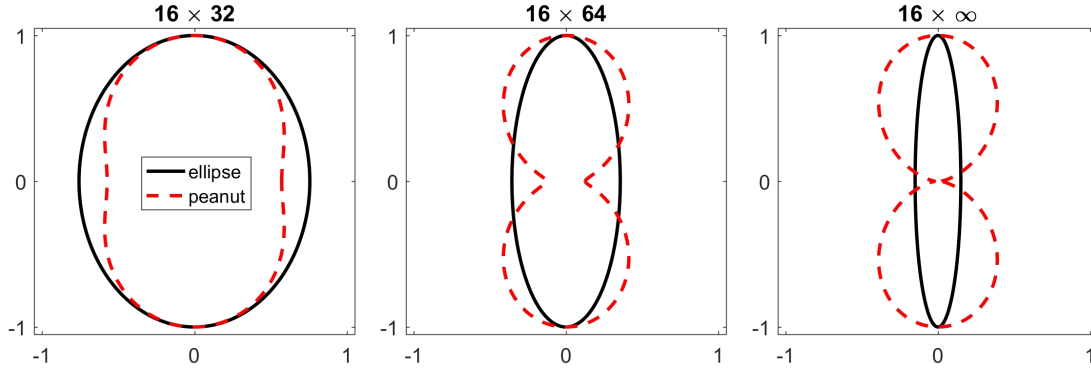


Fig. 6 Diffusion ellipses (black solid line) and peanuts (red-dashed line) representing the anisotropic cell migration for the 16×32 , 16×64 and $16 \times \infty$ micro-ridge arrangements, see Table 2. Note that we renormalise the longer axes to aid comparison between their respective shapes.

553 image of the map $\mathbf{w} \mapsto \mathbf{w}^T \mathbb{D} \mathbf{w}$ for $\mathbf{w} \in S^1$, and relates to the mean-squared displacement in direction \mathbf{w} , $\sigma_{\mathbf{w}}^2$,
 554 via $\sigma_{\mathbf{w}}^2 = 2t \mathbf{w}^T \mathbb{D} \mathbf{w}$ [45]. This gives rise to the *apparent diffusion coefficient in direction \mathbf{w}* ,

$$\text{ADC}_{\mathbf{w}} := \frac{\sigma_{\mathbf{w}}^2}{2t} = \mathbf{w}^T \mathbb{D} \mathbf{w}.$$

555 In particular, given coordinate directions $(1, 0)^T$ and $(0, 1)^T$, we find that the mean squared displacements in
 556 x - and y -directions will be $2t\lambda_x$ and $2t\lambda_y$ respectively. This provides the key for using the data in Table 1:
 557 given the mean velocities in x and y directions and taking a unit time step of 1 minute, we convert to mean
 558 displacements for the x and y directions and in turn estimate the λ 's in (39), the values of which are listed
 559 in Table 2 for each experimental setting. To illustrate some of the anisotropies graphically, we plot diffusion
 560 ellipses and peanuts for the three cases 16×32 , 16×64 and $16 \times \infty$ in Figure 6. As the structure is stretched
 561 along the y - direction we observe progressively thinned-out ellipses/pinched peanuts, reflecting restricted
 562 movement along this axis.

563 For turning rates of the order of 2.5/min and a tracking timeframe of 400 minutes, each cell turns on
 564 average 1000 times across its track. Given an average speed of $0.5 \mu\text{m}/\text{min}$, each particle travels about 200
 565 μm in this timeframe, suggesting this to be a suitably macroscopic scale. We subsequently plot solutions
 566 to the FAAD model on this spatial and temporal scale, plotting the evolving distribution for 10 individuals
 567 presumed to have started at the origin. Exploiting the spatially uniform nature of the environment, solutions
 568 will simply be governed by the fundamental solution (41), which we plot in Figure 7 at $t = 100$ and $t = 400$
 569 for the same three cases 16×32 , 16×64 and $16 \times \infty$. Consistent with the diffusion ellipses, the highest
 570 degree of environmental anisotropy generates a quasi-one dimensional spread of the cells along the y -axis.
 571 We note that there is no direct information in [25] that allows us to directly compare these plots to their data,
 572 and therefore this represents a prediction of the expected population distribution.

573

574 We can turn the argument full circle and use the measured data to estimate cell movement parameters that
 575 would be required in the underlying velocity-jump process: speed s , turning rate μ , and concentration param-
 576 eter κ of the bimodal von-Mises distribution (14). We should note that this is predicated on an *assumption*
 577 of the individual-level behaviour: i.e. that cells orient according to a bimodal von-Mises distribution. In the

Case ($\mu\text{m} \times \mu\text{m}$)	Ridge height (μm)	Speed \pm error ($\mu\text{m}/\text{min}$)	$\lambda_x \pm$ error ($\mu\text{m}^2/\text{min}$)	$\lambda_y \pm$ error ($\mu\text{m}^2/\text{min}$)	Turning rate (/min)	Anisotropy Parameter
12 x 24	3	0.78 ± 0.027	0.072 ± 0.0057	0.17 ± 0.015	2.53	2.57
12 x 48	3	1.01 ± 0.045	0.039 ± 0.0039	0.41 ± 0.041	2.29	10.79
12 x ∞	3	0.59 ± 0.029	0.0032 ± 0.00040	0.16 ± 0.016	2.17	49.49
16 x 32	3	0.9 ± 0.03	0.12 ± 0.010	0.21 ± 0.017	2.48	1.96
16 x 64	3	1.0 ± 0.039	0.048 ± 0.0047	0.38 ± 0.033	2.34	8.32
16 x ∞	3	0.84 ± 0.0072	0.0072 ± 0.00080	0.32 ± 0.029	2.15	44.84
24 x 48	3	0.55 ± 0.027	0.034 ± 0.0039	0.088 ± 0.010	2.47	2.89
24 x 96	3	0.58 ± 0.022	0.020 ± 0.0024	0.12 ± 0.0098	2.40	6.42
24 x ∞	3	0.52 ± 0.028	0.0072 ± 0.00084	0.12 ± 0.013	2.20	16.47
12 x 24	10	0.65 ± 0.026	0.055 ± 0.0053	0.11 ± 0.011	2.63	2.10
12 x 48	10	0.83 ± 0.046	0.016 ± 0.0023	0.29 ± 0.033	2.25	18.28
12 x ∞	10	0.61 ± 0.032	0.00081 ± 0.00012	0.18 ± 0.019	2.05	224.22
control	0	0.63 ± 0.025	0.072 ± 0.0072	0.085 ± 0.014	2.53	0.83

Table 2 Speed and diffusion coefficients λ_x and λ_y from the data from Jeon et al. [25]. We also list the values for the turning rate μ , and the concentration parameter κ of a corresponding bi-modal von-Mises distribution.

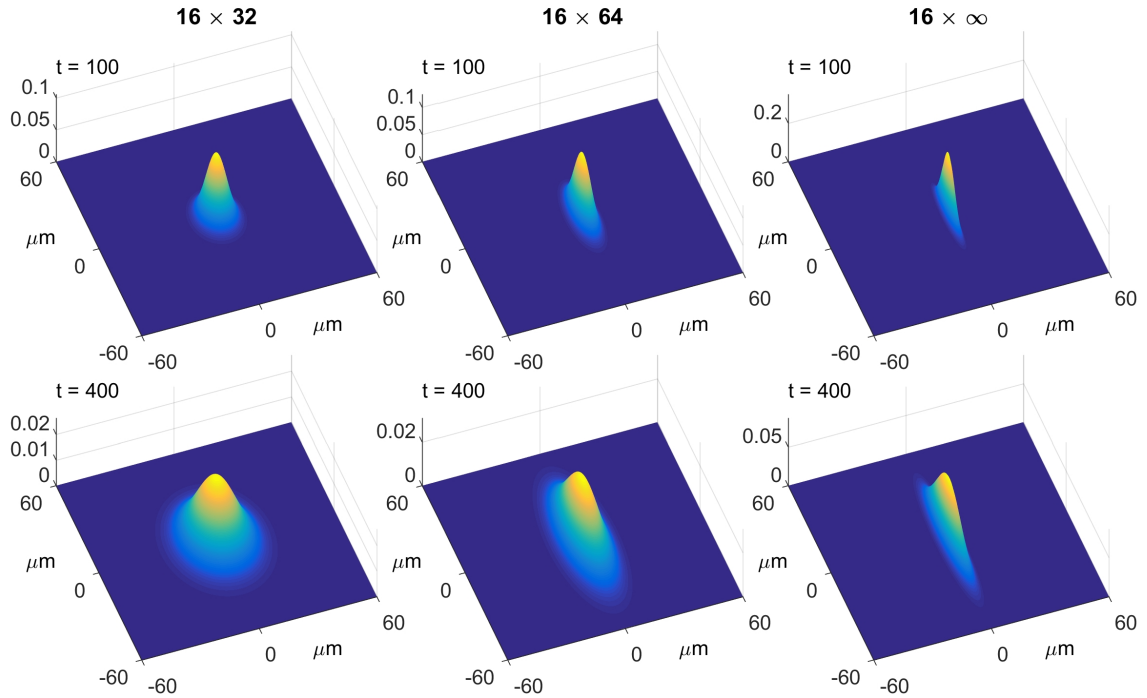


Fig. 7 Population distributions $u(\mathbf{x}, t)$ plotted at (top row) $t = 100$ and (bottom row) $t = 400$ for 10 cells initiated at $\mathbf{x} = \mathbf{0}$.

578 absence of specific individual-level data, this is of course impossible to state with certainty, yet it is never-

579 theless instructive to show how we can “reverse the process”.

580

581 Recall that, given the symmetric/bidirectional scenario, the drift velocity $\mathbf{a} = 0$ and the macroscopic model
582 becomes the pure fully anisotropic diffusion equation

$$u_t = \nabla \nabla : (\mathbb{D}u),$$

583 with diffusion tensor from (36)

$$\mathbb{D} = \frac{s^2}{\mu} \mathbb{V}_q = \frac{s^2}{2\mu} \left(1 - \frac{I_2(\kappa)}{I_0(\kappa)} \right) \mathbb{I}_2 + \frac{s^2}{\mu} \frac{I_2(\kappa)}{I_0(\kappa)} \mathbf{v} \mathbf{v}^T. \quad (42)$$

584 For now let us write the diffusion tensor in (42) as

$$\mathbb{D} = k_1 \mathbb{I}_2 + k_2 \mathbf{v} \mathbf{v}^T, \quad k_1 = \frac{s^2}{2\mu} \left(1 - \frac{I_2(\kappa)}{I_0(\kappa)} \right), \quad k_2 = \frac{s^2}{\mu} \frac{I_2(\kappa)}{I_0(\kappa)}. \quad (43)$$

585 Since the primary direction of anisotropy is in the y -direction, we have $\mathbf{v} = (0, 1)^T$ and can explicitly com-
586 pute

$$\mathbb{D} = \begin{pmatrix} k_1 & 0 \\ 0 & k_1 + k_2 \end{pmatrix} = \begin{pmatrix} \lambda_x & 0 \\ 0 & \lambda_y \end{pmatrix},$$

587 where we employed (39) for the second equality. Therefore, we obtain two equations relating k_1, k_2 and
588 λ_x, λ_y :

$$k_1 = \lambda_x \quad k_1 + k_2 = \lambda_y.$$

589 Using the expressions for k_1 and k_2 in (43) we find $\text{tr} \mathbb{D} = \lambda_x + \lambda_y = \frac{s^2}{\mu}$, which gives

$$\mu = \frac{s^2}{\lambda_x + \lambda_y}. \quad (44)$$

590 The corresponding values for the turning rate μ are listed in Table (2). Furthermore we can use the previous
591 relations to compute

$$\frac{I_2(\kappa)}{I_0(\kappa)} = \frac{\mu(\lambda_y - \lambda_x)}{s^2}. \quad (45)$$

592 Determining concentration (or anisotropy) parameter κ demands inverting the ratio of modified Bessel func-
593 tions $I_2(\kappa)/I_0(\kappa)$, a monotonically increasing function from 0 to 1 for $\kappa \in [0, \infty)$. We use Wolfram Alpha to
594 invert this function for our data and list the corresponding values in Table (2).

595

596 The turning rate μ is surprisingly consistent between the different experiments, which may reflect that this
597 parameter is (relatively) independent of the form of the substratum (for example, determined mainly by
598 intracellular factors). The anisotropy parameter κ , however, varies over several orders of magnitude with
599 the most anisotropic cases corresponding to those without ridges in the x -direction, as expected. Graphical
600 illustrations of the bimodal von Mises distribution for the three cases 16×32 , 16×64 and $16 \times \infty$ are
601 provided in Figure 8. Higher ridges ($10 \mu\text{m}$) offer even more guidance and, consequently, larger anisotropy:
602 including an extreme of $\kappa = 224$. This upper value effectively reduces the bimodal von Mises distribution
603 to a pair of Delta functions in opposite directions, so that movement is almost completely confined to the
604 one-dimensional y -direction.

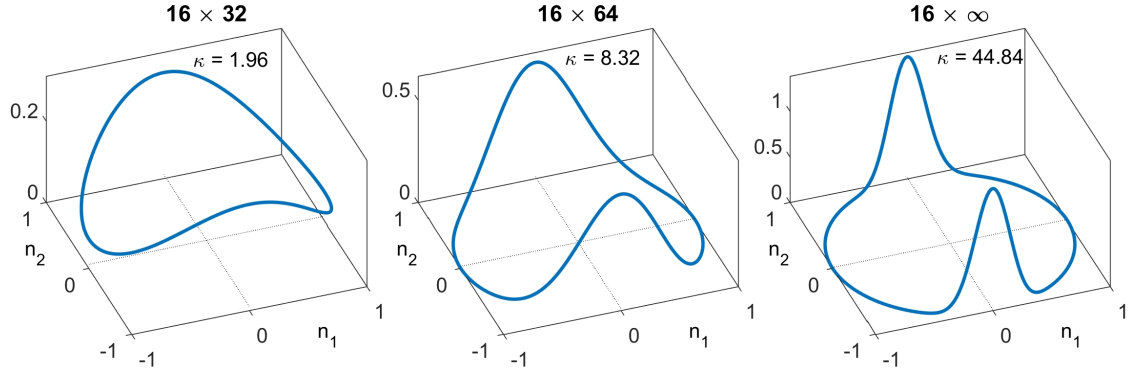


Fig. 8 Bimodal von Mises distributions for the turning distributions of stochastic velocity-jump random walks corresponding to the macroscopic cases in Figure 7.

605 **4.2 Application B: Magnetic Navigation in Loggerhead Hatchlings**

606 Our second application considers hatchling loggerhead turtle navigation, investigating the extent to which
 607 oriented swimming keeps them within the relative safety of the North Atlantic Gyre. Specifically, we extend
 608 the agent-based simulation study of [51], exploiting the computational advantages of the FAAD model to
 609 investigate how different amounts of oriented swimming help to maintain turtle trajectories. We specifically
 610 focus on two critical regions of the Gyre as follows.

- 611 • (NE) a north east Gyre location corresponding to a “corridor” along its northeastern sector, the region
 612 where it breaks into northerly (perilous) and southerly moving streams. We center this region on the point
 613 marked 3 in Figure 2, with its corresponding dataset providing the parameters for orientation.
- 614 • (SW) a south west Gyre location corresponding to a region of the Carribean, where the Gyre branches
 615 into a more northerly stream that remains within the Gyre, or continues west into the Gulf of Mexico.
 616 We center this region on point 7 in Figure 2, with its corresponding dataset providing the parameters for
 617 orientation.

618 In each case we quantitatively assess the extent to which hatchling turtles that are continuously immersed at
 619 some point inside (NE) or (SW) tend to maintain a trajectory within the Gyre. Specifically, for each region
 620 (NE) and (SW) we numerically solve the FAAD equation, as extended to incorporate both an additional drift
 621 (as derived above, see equation (38)) due to currents and a constant (in time) source representing hatchlings
 622 entering the region under investigation. Specifically, defining $u(\mathbf{x}, t)$ to be the hatchling turtle density, we
 623 solve

$$u(\mathbf{x}, t)_t + \nabla \cdot ((\mathbf{a}(\mathbf{x}, t) + \mathbf{b}(\mathbf{x}, t))u(\mathbf{x}, t)) = \nabla \nabla : (\mathbb{D}(\mathbf{x}, t)u(\mathbf{x}, t)) + \gamma \delta_{\mathbf{x}_0}(\mathbf{x}), \quad (46)$$

624 where, in addition to previous definitions, γ represents the rate at which new hatchlings enter the system and
 625 $\delta_{\mathbf{x}_0}$ is the 2D Dirac delta function. The point \mathbf{x}_0 defines the “immersion site” and we set $\mathbf{x}_0 = (25^\circ W, 44.5^\circ N)$
 626 for (NE) and $\mathbf{x}_0 = (56.5^\circ W, 8^\circ N)$ for (SW), respectively denoting points upwards of the general current di-
 627 rection for the regions. Encountered currents $\mathbf{b}(\mathbf{x}, t)$ can vary considerably over time, and we therefore inject
 628 hatchlings continuously into the corridor across a full calendar year (taken to be 2016). Our restriction to the
 629 two-dimensional ocean surface follows from the poor diving abilities of young marine turtles: a maximum

630 dive of the order of 1-2 metres for loggerhead hatchlings [10].

631
632 We define a “success” and a “failure” boundary for each region, removing turtles if they hit either of these
633 boundaries and tracking over time the total numbers that have done so. In the context of the continuous
634 model, this corresponds to setting absorbing boundary conditions along two boundaries. For the (NE) region
635 we define the success boundary along the 42.5°N line and the failure boundary along 46.5°N line; the more
636 northerly line represents turtles moving towards cooler waters and straying from the southerly shifting Gyre.
637 For (SW) the success boundary is set along 18°N line and the failure boundary marked by 64.5°W ; success
638 is implied by a northerly shift with the Gyre, while failure is marked by a westward shift towards the Gulf
639 of Mexico. Of course, the lack of any data makes any such notion of success or failure moot and we cannot
640 equate these boundaries with survival probabilities: they simply provide a proxy to track the tendency to
641 remain within the Gyre.

642
643 To close the computational regions we consider two further boundaries with reflective boundary conditions
644 associated with them, so that there is no net loss across these boundaries. For (NE) we consider the lines
645 $28^\circ\text{W}/12^\circ\text{W}$, and for (SW) the lines $54.5^\circ\text{W}/8^\circ\text{N}$. Note that these lines are all reasonably far from the initial
646 injection site such that, in practice, the vast majority of turtles end up becoming absorbed by one of the
647 success/failure boundaries before hitting one of the reflective boundaries.

648 4.2.1 Data and parametrisation

649 The model demands two specific components that can be drawn from biological data: the ocean cur-
650 rents $\mathbf{b}(\mathbf{x}, t)$ for the passive drift vector field and navigation/movement parameters for hatchling active
651 movement. Velocity fields for ocean currents are obtained from HYCOM (the global HYbrid Coordi-
652 nate Ocean Model, [6]), an ocean forecasting model forced by wind speed, heat flux and numerous other
653 factors that has been subsequently assimilated with field measurements (from satellites, floats, moored
654 buoys etc) to generate post-validated output. The resolution of HYCOM data ($1/12^\circ$ and day to day) al-
655 lows it to reproduce both the large scale persistent currents and localised phenomena such as eddies. Note
656 that the surface/near-surface swimming behaviour of young turtles allows us to restrict to the (2D) upper-
657 most layer of HYCOM datasets. HYCOM data for each of regions (NE) and (SW) was downloaded from
658 <http://pdrc.soest.hawaii.edu/data/data.php>, accessed during June/July 2017. Note that
659 for computations, HYCOM data has been interpolated from its native resolutions ($1/12^\circ$ and day-day) to the
660 spatial/temporal resolution required by the numerical code via standard linear interpolation schemes.

661
662 Defining the active movement component to motion requires specifying the speed/turning rate (s, λ) param-
663 eters and the concentration/dominant direction (κ, \mathbf{v}) parameters demanded by the von Mises distribution.
664 Hatchlings are capable of sustaining speeds of 0.72 km/hr (see [51] and references therein) and, based on
665 this, we suppose the average daily swim length varies from 0-10 km/day, corresponding to between 0 and
666 ~ 14 hours per day of active swimming. Of course, whether a hatchling would be capable of maintaining
667 active swimming at the upper end of this spectrum is somewhat debatable. For the turning rate, we assume a
668 value of 50 per day, although it is noted that modifying this parameter has very little bearing on the overall
669 results. Given this turning rate and assuming each turtle remains in the simulated region for the order of 100
670 days, we obtain an average of 5000 turns per trajectory. For average swimming speeds ranging between 0-10
671 km/day, turtles swim up to 1000 km over the simulation timecourse, implying spatial scales of the order 100-
672 1000 km as suitably macroscopic. We remark that the comparisons between the individual and continuous

673 simulations suggest the veracity of the continuous limit as a suitable approximation.

674

675 Concentration parameters/dominant directions can be drawn directly from the hatchling orientation datasets
 676 illustrated in Figure 2. For region (NE) we utilise the dataset indicated by position 3: fitting a von Mises
 677 distribution via standard methods (e.g. see [2]) allow us to obtain estimates $\kappa_{NE} \approx 0.874$ and $\mathbf{v}_{NE} \approx$
 678 $(0.307, -0.952)$, the latter representing a true bearing of 162° . The region (SW) employs position 7 and
 679 yields $\kappa_{SW} \approx 0.797$ and $\mathbf{v}_{SW} \approx (0.070, 0.998)$, representing a true bearing of 4° . We assume these values are
 680 constant in space and time over the respective regions.

681 4.2.2 Results

682 In Figure 9 we compare the density distribution predicted by the parametrised FAAD model (46) with a
 683 particle distribution obtained through individual-based simulations of the stochastic velocity-jump process.
 684 The close correlation between the continuous density distribution (as reflected by the colormap) and the
 685 distribution of individual particles (white dots) indicates that the FAAD model provides a highly acceptable
 686 approximation for the turtle distribution. Further simulations (not shown) confirm this close correspondence,
 687 and we therefore exploit the FAAD model for its computational advantages in the subsequent simulations.

688

689 Figure 10 compares density distributions for the same region at the same time points under three choices for
 690 the amount of active swimming: 0 km/day (i.e. only passive drifting occurs), 2 km/day and 10 km/day. A
 691 shift towards a greater amount of active swimming has a clear impact on the density distribution, pushing
 692 it in an expected southerly direction such that a greater density becomes absorbed by the “success” boundary.
 693

694 Finally, we plot the results from a more extended analysis, following a parameter sweep for each of the two
 695 regions, classifying the data obtained in terms of the following simple “success measure”:

$$\text{Success at time } T = \frac{\text{Total density hitting success boundary by time } T}{\text{Total density hitting success and failure boundaries by time } T}.$$

696 The above clearly approaches 1 for a successful population and 0 for an unsuccessful population. In the sim-
 697 ulations here we set $T = 500$ for a population continuously released at \mathbf{x}_0 from $t = 0$ (midnight, 01/01/2016)
 698 to the end of 2016 ($t = 366$); the continuation until $T = 500$ ensures that by the end of the simulation only a
 699 negligible fraction of the released population has failed to hit one of the absorbing boundaries. Simulations
 700 are plotted in Figure 11 for each of the two regions, under a range of daily active swimming distances and
 701 for three values of the concentration parameter: the value obtained by the data fitting and perturbations of
 702 $\times 2$ and $\times 1/2$ these values. The simulations clearly show that increasing the amount of active swimming, or
 703 increasing the certainty of orientation, nudges a greater proportion of the population towards the successful
 704 boundary, supporting the hypothesis that oriented responses can help maintain hatchling movement within
 705 the Gyre (e.g. [28, 51]). Extensions of the study to consider movement throughout the full circulatory path
 706 would allow more detailed evaluations into the extent to which oriented swims aid route maintenance: we
 707 remark that this would be a focus for a future study and refer to [28] for such an analysis for an individual-
 708 based model.

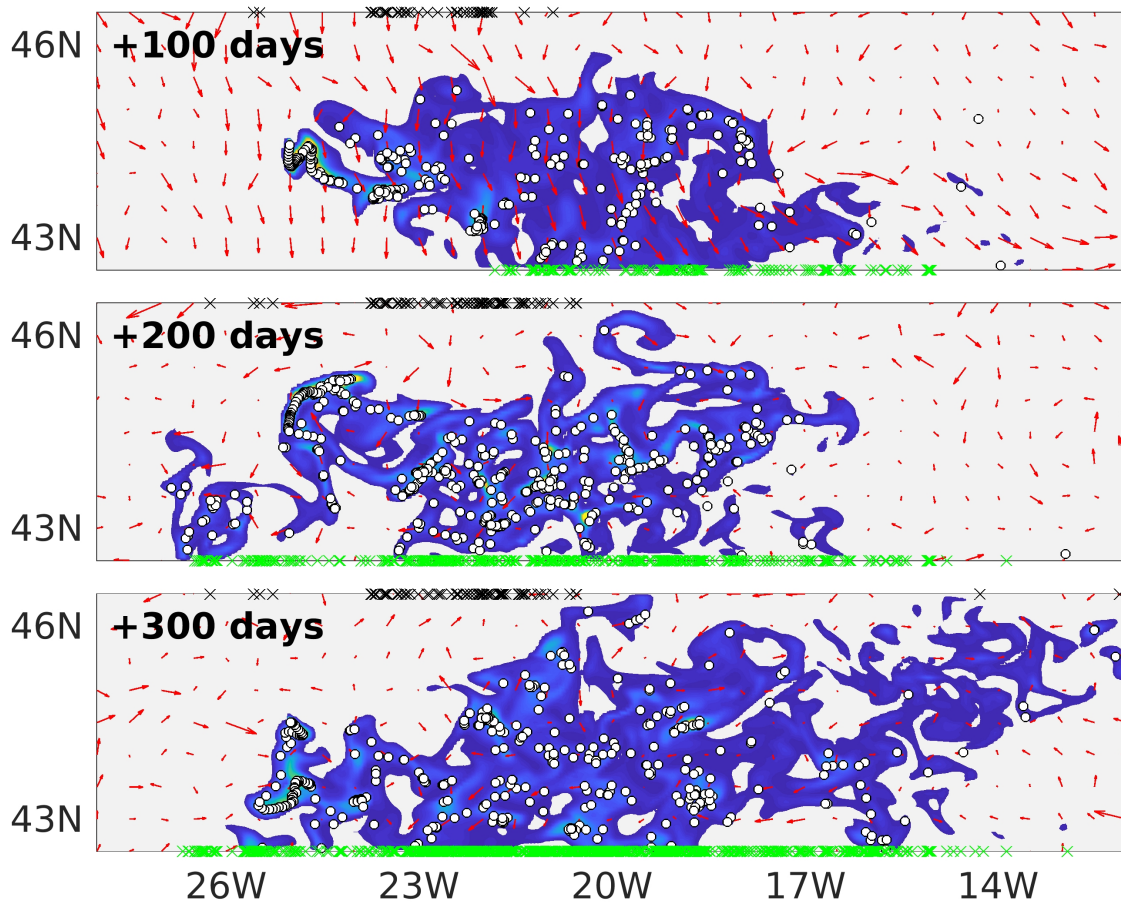


Fig. 9 Comparison between the FAAD model (46) and individual-based stochastic simulations of the velocity-jump model for the problem of North Atlantic turtle hatchling movement. In each frame we plot both the continuous population density distribution $u(\mathbf{x}, t)$ (reflected by the colour map, where grey indicates negligible density and blue to yellow reflects increasing density) and the individual dots generated by the velocity-jump simulations. Here, top and bottom boundaries respectively define the “failure” and “success” boundaries, and the individual particles are colour coded according to whether they are still moving (white dots) or have hit either the failure (black crosses) or success (green crosses) boundary. Underlying ocean currents are indicated by the red arrows. For this simulation we use region (NE) and release particles continuously from position $\mathbf{x}_0 = (25^\circ\text{W}, 44.5^\circ\text{N})$ with $\gamma = 5/\text{day}$. The total daily swim is set at $s = 2 \text{ km/day}$, with $\lambda = 50/\text{day}$, $\kappa_{NE} \approx 0.874$ and $\mathbf{v}_{NE} \approx (0.307, -0.952)$. Note that the von Mises distribution for these values is visualised by the dashed red line in the inset figure to the left hand frame of Figure 11. Simulations (in terms of ocean currents utilised) start on 01/01/2016 (midnight) with solutions displayed on the days following as indicated.

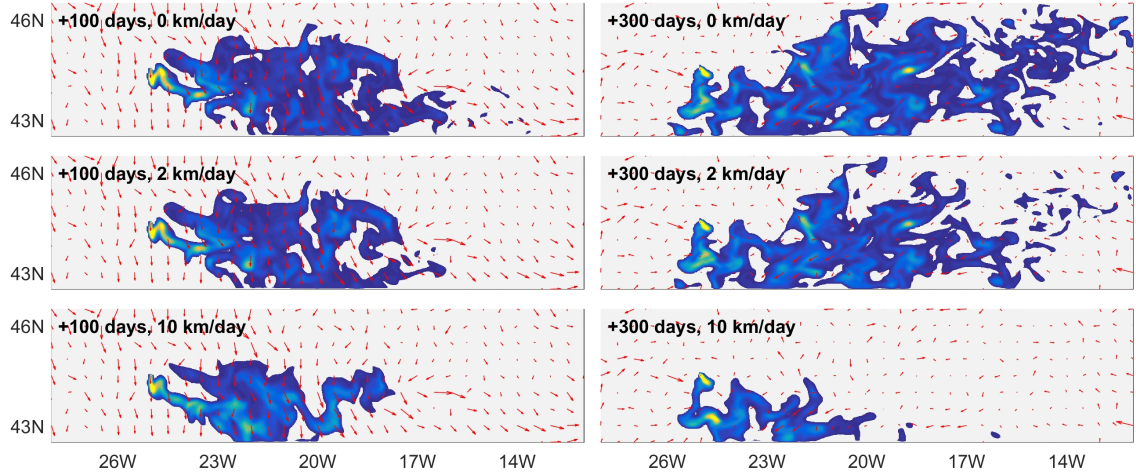


Fig. 10 Comparison of population density distributions under varying amounts of active swimming per day. In each frame we plot the turtle density distribution (color density map, as described in Figure 9) at the two separate times (left) +100 days and (right) +300 days for (top row) $s = 0$ km/day, (middle row) $s = 2$ km/day and (bottom row) $s = 10$ km/day. The strength and direction of ocean currents is indicated by the red arrows. All other parameters and details as in Figure 9.

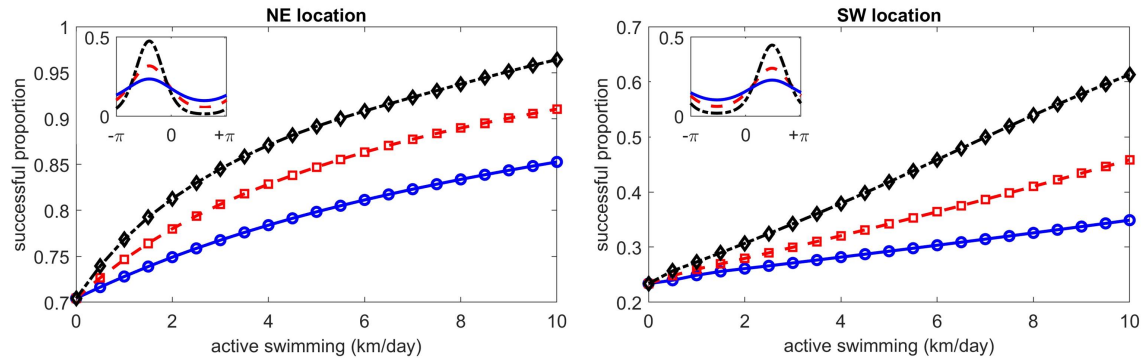


Fig. 11 Success is plotted as a function of daily swimming distance for the two regions and for different concentration parameters. All other parameters and details as in Figure 9. Red dashed line indicates a choice of κ as taken directly from the data fitting, with blue solid and black dot-dashed respectively showing choices of $\times 2$ and $\times 1/2$ these values. Inset plots the corresponding von Mises distributions used for each simulation set.

709 5 Conclusions

710 In this chapter we have described the use of fully-anisotropic advection-diffusion models as a way of mod-
 711 elling animal and cell movement behaviour. We have described the derivation of these models from two
 712 fundamental stochastic random walks, position-jump and velocity-jump processes, thereby connecting the
 713 macroscopic parameters and terms to the statistical inputs at the individual level. Utilising two distinct
 714 datasets, we have shown how the models can be parametrised either directly at the population level, or

715 by starting at the individual/stochastic random walk model. Beyond the applications presented here, we note
 716 that similar methods have been applied in a number of other applications in ecology and cell movement,
 717 including seismic-line following behaviour of wolves and caribou populations [33, 22], butterfly hilltopping
 718 [44], and anisotropic glioma growth [45, 56].

719 **Acknowledgements:** KJP would like to acknowledge the Politecnico di Torino for the Visiting Professor
 720 award. TH is grateful to the Politecnico di Torino for their hospitality. TH is supported through a discovery
 721 grant of the Natural Science and Engineering Research Council of Canada (NSERC), an Oberwolfach (MFO)
 722 Simons Foundation Visiting Professorship and the Edinburgh Mathematical Society.

723 References

- 724 1. Alt, W.: Biased random walk model for chemotaxis and related diffusion approximation. *J. Math. Biol.* **9**, 147–177 (1980)
- 725 2. Batschelet, E.: *Circular Statistics in Biology*. Academic Press, London (1981)
- 726 3. Bellomo, N., Schiavo, M.: *Lecture Notes on the Mathematical Theory of Generalized Boltzmann Methods*. World Scien-
 727 tific, Singapore (2000)
- 728 4. Berens, P.: Circstat: a MATLAB toolbox for circular statistics. *J. Stat. Softw.* **31**, 1–21 (2009)
- 729 5. Berg, H.: *Random Walks in Biology*. Princeton University Press (1983)
- 730 6. Bleck, R.: An oceanic general circulation model framed in hybrid isopycnic-cartesian coordinates. *Ocean Mod.* **4**, 55–88
 731 (2002)
- 732 7. Cagnacci, F., Boitani, L., Powell, R.A., Boyce, M.S.: Animal ecology meets GPS-based radiotelemetry: a perfect storm of
 733 opportunities and challenges. *Phil. Trans. R. Soc. B* **365**, 21572162 (2010)
- 734 8. Cercignani, C., Illner, R., Pulvirenti, M.: *The Mathematical Theory of Diluted Gases*. Springer, New York (1994)
- 735 9. Codling, E.A., Plank, M.J., Benhamou, S.: Random walk models in biology. *J. Roy. Soc. Interface* **5**, 813–834 (2008)
- 736 10. Davenport, J. and Clough, W.: Swimming and diving in young loggerhead sea turtles (*Caretta caretta L.*). *Copeia*, **1986**,
 737 53–57 (1986)
- 738 11. Dawes, A., Iron, D.: Cortical geometry may influence placement of interface between par protein domains in early
 739 *caenorhabditis elegans* embryos. *J. Theor. Bio.* **333**, 27–37 (2013)
- 740 12. Deutsch, A., Dormann, S.: *Cellular Automaton Modeling of Biological Pattern Formation: Characterization, Applications,*
 741 *and Analysis*. Birkaeuser, Boston (2005)
- 742 13. Dickinson, R.B., Guido, S., Tranquillo, R.T.: Biased cell migration of fibroblasts exhibiting contact guidance in oriented
 743 collagen gels. *Ann. Biomed. Eng.* **22**, 342–356 (1994)
- 744 14. Dunn, G.A., Heath, J.P.: A new hypothesis of contact guidance in tissue cells. *Exp. Cell Res.* **101**, 1–14 (1976)
- 745 15. Fuxjager, M.J., Eastwood, B.S., Lohmann, K.J.: Orientation of hatchling loggerhead sea turtles to regional magnetic fields
 746 along a transoceanic migratory pathway. *J. Exp. Biol.* **214**, 2504–2508 (2011)
- 747 16. Gritsenko, P., Ilina, O., Friedl, P.: Interstitial guidance of cancer invasion. *J. Pathol.* **226**, 185–199 (2012)
- 748 17. Gritsenko, P., Leenders, W., Friedl, P.: Recapitulating in vivo-like plasticity of glioma cell invasion along blood vessels and
 749 in astrocyte-rich stroma. *Histochem. Cell Biol.* (2017). doi: 10.1007/s00418-017-1604-2
- 750 18. Hadeler, K., Hillen, T., Lutscher, F.: The Langevin or Klein-Kramers approach to biological modeling. *Math. Models*
 751 *Meth. Appl. Sci.* **14**(10), 1561–1583 (2004)
- 752 19. Hanahan, D., Weinberg, R.: Hallmarks of cancer: The next generation. *Cell* **144**, 646–674 (2011)
- 753 20. Hillen, T.: M^5 mesoscopic and macroscopic models for mesenchymal motion. *J. Math. Biol.* **53**, 585–616 (2006)
- 754 21. Hillen, T., Othmer, H.: The diffusion limit of transport equations derived from velocity jump processes. *SIAM J. Appl.*
 755 *Math.* **61**, 751–775 (2000)
- 756 22. Hillen, T., Painter, K.J.: Transport models for movement in oriented habitats and anisotropic diffusion. In: Lewis, M.,
 757 Maini, P., Petrovskii, S. (Eds.), *Dispersal, Individual Movement and Spatial Ecology: A Mathematical Perspective*.
 758 Springer, Heidelberg. p. 46 (2013)
- 759 23. Hillen, T., Painter, K.J., Swan, A.C., Murtha, A.D.: Moments of von Mises and Fisher distributions and applications. *Math.*
 760 *Biosci. & Eng* **14**, 673–694 (2017)
- 761 24. Hundsdorfer, W., Verwer, J.G.: Numerical solution of time-dependent advection-diffusion-reaction equations, vol. 33.
 762 Springer Science & Business Media (2003)

- 763 25. Jeon, H., Hidai, H., Hwang, D.J., Healy, K.E., Grigoropoulos, C.P.: The effect of microscale anisotropic cross patterns on
764 fibroblast migration. *Biomaterials* **31**, 4286–4295 (2010)
- 765 26. Keener, J., Sneyd, J.: *Mathematical Physiology*. Springer (1994)
- 766 27. Lohmann, K.J., Cain, S.D., Dodge, S.A., Lohmann, C.M.F.: Regional magnetic fields as navigational markers for sea
767 turtles. *Science* **294**, 364–366 (2001)
- 768 28. Lohmann, K.J., Putman, N.F., Lohmann, C.M.F.: The magnetic map of hatchling loggerhead sea turtles. *Curr. Opin.*
769 *Neurobiol.* **22**, 336–342 (2012)
- 770 29. Luschi, P.: Long-distance animal migrations in the oceanic environment: orientation and navigation correlates. *ISRN Zool.*
771 (2013)
- 772 30. Lutscher, F., Pachepsky, E., Lewis, M.: The effect of dispersal patterns on stream populations. *SIAM J. Appl. Math.* **65**,
773 1305–1327 (2005)
- 774 31. Mardia, K., Jupp, P.: *Directional Statistics*. Wiley and Sons (2000)
- 775 32. McKenzie, H., Lewis, M., Merrill, E.: First passage time analysis of animal movement and insights into the functional
776 response. *Bull. Math. Biol.* **71**, 107–129 (2009)
- 777 33. McKenzie, H.W., Merrill, E.H., Spiteri, R.J., Lewis, M.A.: How linear features alter predator movement and the functional
778 response. *Interface focus* **2**, 205–216 (2012)
- 779 34. Moorcroft, P., Lewis, M.: *Mechanistic Home Range Analysis*. Princeton University Press, Princeton (2006)
- 780 35. Murray, J.: *Mathematical Biology. I: An Introduction*, 3rd edn. Springer-Verlag, New York (2002)
- 781 36. Murray, J.D.: *Mathematical biology II: Spatial models and biochemical applications*, Springer-Verlag, New York (2003)
- 782 37. Okubo, A., Levin, S.: *Diffusion and Ecological Problems: Modern Perspectives*. Springer (2002)
- 783 38. Othmer, H., Dunbar, S., Alt, W.: Models of dispersal in biological systems. *J. Math. Biol.* **26**, 263–298 (1988)
- 784 39. Othmer, H.G., Stevens, A.: Aggregation, blowup, and collapse: the ABC’s of taxis in reinforced random walks. *SIAM J.*
785 *Appl. Math.*, **57**, 1044–1081 (1997).
- 786 40. Othmer, H., Hillen, T.: The diffusion limit of transport equations II: Chemotaxis equations. *SIAM J. Appl. Math.* **62**,
787 1122–1250 (2002)
- 788 41. Othmer, H.G., Xue, C.: The mathematical analysis of biological aggregation and dispersal: progress, problems and perspec-
789 tives. In: Lewis, M., Maini, P., Petrovskii, S. (Eds.), *Dispersal, Individual Movement and Spatial Ecology: A Mathematical*
790 *Perspective*. Springer, Heidelberg, 79–127 (2013)
- 791 42. Painter, K.J.: Modelling migration strategies in the extracellular matrix. *J. Math. Biol.* **58**, 511–543 (2009)
- 792 43. Painter, K.J., Hillen, T.: Navigating the flow: Individual and continuum models for homing in flowing environments. *Royal*
793 *Soc. Interface* **12**, 20150,647 (2015)
- 794 44. Painter, K.J.: Multiscale models for movement in oriented environments and their application to hilltopping in butterflies.
795 *Theor. Ecol.* **7**, 53–75 (2014)
- 796 45. Painter, K.J., Hillen, T.: Mathematical modelling of glioma growth: the use of diffusion tensor imaging (DTI) data to
797 predict the anisotropic pathways of cancer invasion. *J. Theor. Biol.* **323**, 25–39 (2013)
- 798 46. Patlak, C.: Random walk with persistence and external bias. *Bull. Math. Biophys.* **15**, 311–338 (1953)
- 799 47. Perthame, B.: *Transport Equations in Biology*. Birkhäuser (2007)
- 800 48. Preziosi, L. (ed.): *Cancer Modelling and Simulation*. Chapman Hall/CRC Press (2003)
- 801 49. Provenzano, P.P., Eliceiri, K.W., Campbell, J.M., Inman, D.R., White, J.G., Keely, P.J.: Collagen reorganization at the
802 tumor-stromal interface facilitates local invasion. *BMC medicine* **4**, 38 (2006)
- 803 50. Putman, N.F., Endres, C.S., Lohmann, C.M.F., Lohmann, K.J.: Longitude perception and bicoordinate magnetic maps in
804 sea turtles. *Curr. Biol.* **21**, 463–466 (2011)
- 805 51. Putman, N.F., Verley, P., Shay, T.J., Lohmann, K.J.: Simulating transoceanic migrations of young loggerhead sea turtles:
806 merging magnetic navigation behavior with an ocean circulation model. *J. Exp. Biol.* **215**, 1863–1870 (2012)
- 807 52. Saxton, M.J., Jacobson, K.: Single-particle tracking: applications to membrane dynamics. *Ann. Rev. Biophys. & Biomol.*
808 *Struct.* **26**, 373–399 (1997)
- 809 53. Sobel, D.: *Longitude: The true story of a lone genius who solved the greatest scientific problem of his time*. Bloomsbury
810 Publishing USA (1995)
- 811 54. Stevens, A.: The derivation of chemotaxis-equations as limit dynamics of moderately interacting stochastic many particle
812 systems. *SIAM J. Appl. Math.* **61**(1), 183–212 (2000)
- 813 55. Stevens, A., Othmer, H.G.: Aggregation, blowup, and collapse: the ABC’s of taxis in reinforced random walks. *SIAM J.*
814 *Appl. Math.* **57**, 1044–1081 (1997)
- 815 56. Swan, A., Hillen, T., Bowman, J.C., Murtha, A.D.: A patient-specific anisotropic diffusion model for brain tumour spread.
816 *Bull. Math. Biol.* pp. 1–33 (2017)
- 817 57. Turchin, P.: *Quantitative Analysis of Movement*. Sinauer Assoc., Sunderland (1998)
- 818 58. Weickert, J.: *Anisotropic diffusion in image processing*. Teubner, Stuttgart (1998)

819 59. Wolf, K., Müller, R., Borgmann, S., Bröcker, E.B., Friedl, P.: Amoeboid shape change and contact guidance: T-lymphocyte
 820 crawling through fibrillar collagen is independent of matrix remodeling by MMPs and other proteases. *Blood* **102**, 3262–
 821 3269 (2003)

822 **Appendix: Numerical methods**

823 *Stochastic Velocity-Jump Process*

824 The stochastic random walk simulations assume each individual performs a velocity-jump random walk in
 825 either a static (cell movement) or flowing (turtles) medium. Particle motion therefore derives from an ori-
 826 ented and active movement component that describes the individual’s self motility (crawling, swimming,
 827 flying etc), the details of which are encoded in the velocity-jump random walk, and a passive drift due to
 828 movement of the medium (e.g. air or water flow). The passive drift is described by a velocity vector field
 829 $\mathbf{b}(\mathbf{x}, t)$ (\mathbf{x} is position and t is time) that could be either imposed (e.g. obtained from public-domain datasets)
 830 or separately modelled (e.g. Navier-Stokes equation). Note that we implicitly assume that the individuals
 831 have negligible impact on the flow of the surrounding medium.

832

833 For an individual i at position $\mathbf{x}_i(t)$ and time t , travelling with active velocity $\mathbf{v}_i(t) = s(\cos \alpha_i(t), \sin \alpha_i(t))$
 834 where angle $\alpha_i(t)$ denotes the active heading, then at time $t + \Delta t$ (where Δt is small) we have:

$$\begin{aligned} \mathbf{x}_i(t + \Delta t) &= \mathbf{x}_i(t) + \Delta t(\mathbf{v}_i(t) + \mathbf{b}(t, \mathbf{x}_i)); \\ \mathbf{v}_i(t + \Delta t) &= \begin{cases} \mathbf{v}'_i(t + \Delta t) & \text{with probability } \lambda \Delta t, \\ \mathbf{v}_i(t) & \text{otherwise.} \end{cases} \end{aligned} \quad (47)$$

835 where $\mathbf{v}'_i(t + \Delta t)$ is the new velocity chosen at time $t + \Delta t$ if a reorientation has occurred, randomly chosen
 836 according to the given probability distribution for the turning kernel of the velocity jump random walk.

837 The time discretisation Δt used in simulation is suitably small, in the sense that simulations conducted
 838 with smaller timesteps generate near identical results. For the selection of new active headings via the von
 839 Mises distribution we employ code (circ_vmrnd.m) from the circular statistics toolbox [4]. Currents and
 840 the inputs required for the active heading choice are interpolated from the native spatial/temporal resolu-
 841 tions in the saved variables to the individual particle’s continuous position \mathbf{x} and time t via a simple linear
 842 interpolation scheme.

843 *Continuous Model*

844 As described earlier, moment closure analysis for the velocity-jump random walk generates a continuous
 845 model of FAAD form

$$u(\mathbf{x}, t)_t + \nabla \cdot ((\mathbf{a}(\mathbf{x}, t) + \mathbf{b}(\mathbf{x}, t))u(\mathbf{x}, t)) = \nabla \nabla (\mathbb{D}(\mathbf{x}, t)u(\mathbf{x}, t)). \quad (48)$$

846 where $\mathbf{a}(\mathbf{x}, t)$ and $\mathbb{D}(\mathbf{x}, t)$ depend on the statistical inputs of the random walk (mean speed, turning rates,
 847 moments of the turning distribution).

848 Numerical methods for solving (48) are adapted from our previous studies (e.g. see [43]). We adopt a
849 simple Method of Lines (MOL) approach, first discretising in space (using a fixed lattice of space Δx) to
850 create a large system of ordinary differential equations (ODEs) which are subsequently integrated over time.
851 The “fully anisotropic” diffusion term, is expanded into an advective and standard anisotropic-diffusion
852 component. This advective component, along with advection terms arising from ocean currents and active
853 directional swimming, are solved via a third-order upwinding scheme, augmented by flux-limiting to ensure
854 positivity of solutions (e.g. see [24]). The choice of finite-difference discretisation for the anisotropic diffu-
855 sion term is more specific: naive discretisations can lead to numerical instability for sufficiently anisotropic
856 scenarios (high κ values). The method of [58] allows greater flexibility in the choice of κ : in this scheme,
857 finite difference derivatives are calculated and combined along distinct axial directions: the axes of the dis-
858 cretisation lattice and the major and minor axes of the ellipse corresponding to the anisotropic diffusion
859 tensor. Under the moderate levels of anisotropy encountered here we obtain a stable scheme. Time discreti-
860 sation here is performed via a simple forward Euler method with a suitably small time step.